

CALCIUM IMAGING WITH THREE-PHOTON MICROSCOPY IN THE MOUSE  
BRAIN

A Dissertation

Presented to the Faculty of the Graduate School  
of Cornell University

In Partial Fulfillment of the Requirements for the Degree of  
Doctor of Philosophy

by

Tianyu Wang

August 2018

© 2018 Tianyu Wang

# CALCIUM IMAGING WITH THREE-PHOTON MICROSCOPY IN THE MOUSE BRAIN

Tianyu Wang, Ph. D.

Cornell University 2018

Calcium imaging posed both opportunities and challenges for three-photon microscopy. With the development of genetically encoded calcium indicators, optical imaging has enabled *in vivo* activity recordings from increasingly large neuronal populations with high spatial and temporal resolution. The synergy between calcium imaging and three-photon microscopy can potentially allow functional imaging beyond the depth limit of two-photon microscopy. However, the transition of three-photon microscopy from structural to functional imaging of high temporal resolution requires orders of magnitude stronger signal. The challenge was eventually overcome by the optimization of three-photon microscopy and the improvement of calcium indicators and their genetic expression. Currently, the technology has been adopted by many researchers for biological and neuroscience studies.

In this thesis, the performance of three-photon microscopy with 1300-nm excitation and two-photon microscopy with 920-nm excitation are quantified and compared for *in vivo* imaging of GCaMP6s-labeled neurons. 1300-nm three-photon microscopy is more suited for imaging in the deep cortex of the mouse brain or beyond because it is more power-efficient for signal generation and has significantly higher signal-to-background ratio. These advantages are the results of the reduced

light attenuation at the longer excitation wavelength and the improved three-dimensional confinement by high order nonlinear excitation. Furthermore, we demonstrated three-photon calcium imaging of  $\sim 150$  GCaMP6s-labeled neurons in the mouse hippocampus at  $\sim 1$ -mm depth within an intact mouse brain. The imaging achieved 8.5 frame/s speed and  $200 \times 200 \mu\text{m}$  field-of-view. With  $\sim 50$  mW average power at 800 kHz repetition rate, we were able to image the same regions in the hippocampus of several animals over multiple days, which manifested the safety and consistency of the method. Three-photon microscopy also finds another surprising application in imaging through the intact mouse skull. Compared to two-photon-excitation, even with the same long excitation wavelength and imaging system, three-photon-excitation significantly improves optical sectioning in presence of the skull-induced scattering and aberration. Through the intact adult mouse skull, we demonstrated three-photon imaging of vasculature at  $>500 \mu\text{m}$  depth, and GCaMP6s-calcium imaging over weeks in cortical layers 2/3 and 4 in awake mice, with 8.5 frames/s and hundreds of micrometers field-of-view.

## BIOGRAPHICAL SKETCH

Tianyu Wang was born on September 20, 1990, to his young parents who just moved to Shanghai a couple years ago to work as engineers. Although the parents did not have a clear future plan for their son, they offered the environment for the kid to explore his own interest. When Tianyu first read about the solar system, human skeleton, and the theory of evolution in an encyclopedia bought to him, he was mind-blown and very fascinated by the clarity and the extent of details people already knew about those subjects, which he never perceived directly himself. With this early impression, he got interested in science in the school, and eventually realized that it was the power of abstract thinking based on facts that enabled people to see things on totally different scales and dimensions than their day-to-day living environments.

He enrolled in Shanghai Jiao Tong University for college in 2008 with electric engineering as the major. However, he was frustrated at the extremely pragmatic pedagogy, which gave very little attention to how concepts are formed and experiments are conceived, but seemed to feed students everyday with random new facts and tricks. He had to spend time to form a coherent picture of physics on his own, in many cases aided by Richard Feynman's lecture notes. In 2010, he transferred to Cornell University to pursue better research opportunities. During the next two years, he majored in biological engineering, yet still struggled to find the right research experience. He expressed a lot interest in system biology after reading Hodgkin-Huxley's paper on action potential, especially on dynamical systems

described by differential equations. However, the actual research project he was given at the moment was to track cells manually on a computer screen. He was obsessed with developing and optimizing a computer algorithm to do the work, which he considered successful in the end. He stayed at Cornell for PhD program, and joined Professor Chris Xu's lab in 2013. Even though the path of research had not been smooth, small progresses have been made over time. After finishing his thesis on three-photon calcium imaging, he is again standing at the crossroad of life.

## ACKNOELEDGEMENTS

I would like to take this opportunity to thank the colleagues who have helped with my research or contributing to a good research environment, as well as friends who have been of positive influence in my life.

First of all, I would like to thank to my advisor Chris Xu, for his clear direction and excellent vision of research impacts. He sets a role model as a very diligent professor who ensures the financial supply for research, always responds immediately to work related issues, and scrutinizes all the experimental results. Next, I am grateful to my committee members, Frank Wise and Nozomi Nishimura, who are always willing to listen to and provide advices to my questions and problems.

Next, thanks to the colleagues who I have spent years working with, especially Dimitre Ouzounov, from whom I learned how to perform optical experiments properly in this lab, not forgetting to mention that he is a trustable colleague with excellent work ethics and an emotionally stable presence in the lab. I also would like to thank Mengran Wang and Chunyan Wu for their timely assistance which were indispensable for the success of the projects, and also for bearing up my immature personality from time to time. I would like to mention Fei Xia and Aaron Mok for their assistance and supportiveness in running lab affairs. During my stay at Xu group, I enjoyed academic/casual/gossip conversations with Kriti Charan, David Huland, Adam Straub, David Sinefeld, Bo Li, Najva Akbari, and Thomas Ciavatti. It was very pleasant to have you in accompany. In addition, I would like to thank my collaborators, Jacob Reimer, Yu-Ting Cheng, Jean Cruz Hernandez and Danielle Feng, some for their

professional help and some for their joyful characters. I also owe my thanks to our department administrators Cynthia Reynolds and Donna Mazza, who always stand on the students' side and helped me to go through a couple crises.

Outside the lab, I wish to thank people who have made positive influence on my life trajectory. Zhanwei Liu and Logan Wright in Wise group are the few who I share similar research tastes with. As more independent researchers and forerunners, they are generous enough to share their perspectives on many topics, which helps to expand my horizon. I am also grateful to my peers Yi Jiang, Yi Wen, Chengyu Liu, and Zhen Chen, with whom I have cultivated my hobby in board games. I will also remember Triphammer cooperative, where I lived more than 4 years, for life experiences nowhere else to find and some friendship probably will last lifelong.

Last but not least, I owe a lot to my parents for their unconditional support for my career choice and patience for all my trial and errors over the years.

## TABLE OF CONTENTS

BIOGRAPHICAL SKETCH.....	v
ACKNOELEDGEMENTS.....	vii
TABLE OF CONTENTS .....	ix
LIST OF FIGURES.....	xi
LIST OF TABLES .....	xiii
<b>1 INTRODUCTION .....</b>	<b>1</b>
1.1 Multi-photon Microscopy.....	1
1.2 Three-photon Microscopy .....	3
1.3 Calcium Imaging .....	5
1.4 Optical Properties of the Brain Tissue.....	6
1.5 Considerations on Deep Tissue Imaging.....	9
<b>2 THE METHODOLOGY OF THREE-PHOTON CALCIUM IMAGING... 11</b>	
2.1 Excitation Sources and Microscope Setup .....	11
2.1.1 Excitation Sources.....	11
2.1.2 Microscope .....	13
2.1.3 Imaging Configuration and Analysis.....	16
2.2 Shot-noise limited Microscope Performance and Quantification of Photon Counts from Images .....	17
2.3 Calculation of the Minimum Signal for Spike Detection based on the Characteristics of the Calcium Indicator .....	19
<b>3 COMPARISON BETWEEN TWO-AND THREE-PHOTON CALCIUM IMAGING DEEP IN THE DENSELY LABELED MOUSE BRAIN..... 22</b>	
3.1 Time-division Multiplexing for Simultaneous Two- and Three-photon Imaging 22	
3.2 Correlation between Two- and Three-photon Calcium Imaging Traces in the Shallow Cortex .....	24
3.3 Effective Attenuation Length of 1320 nm and 920 nm in the Mouse Brain 25	
3.4 Signal Yield per Excitation Pulse on Fluorescein and GCaMP6s.....	28
3.5 Comparison of Signal-to-background Ratio in Deep Cortex .....	32
3.6 Estimate of Nonlinear Damage Threshold by 1320-nm Three-photon Microscopy.....	34
3.7 Estimation of Thermal Damage Threshold by 1320-nm Three-photon Microscopy by Monte Carlo Simulation .....	35
3.8 Optimization of System Parameters for Deep Imaging.....	37
<b>4 THREE-PHOTON CALCIUM IMAGING IN THE MOUSE HIPPOCAMPUS .....</b>	<b>40</b>

4.1	In vivo Three-photon Calcium Imaging of GCaMP6s Neurons in the Hippocampus in Intact Mouse Brains .....	41
4.2	Damage Consideration of Three-photon Calcium Imaging .....	48
4.3	Conclusions .....	51
<b>5</b>	<b>THREE-PHOTON CALCIUM IMAGING THROUGH THE INTACT MOUSE SKULL.....</b>	<b>52</b>
5.1	The Scientific Significance and the Status Quo of Through-skull Imaging .....	52
5.2	Three-photon Excitation Enhances Optical Sectioning through the Intact Mouse Skull.....	54
5.3	Through-Skull Neuronal Structural and Functional Imaging by Three-photon Microscopy .....	62
5.4	Longitudinal Three-photon Through-skull Calcium Imaging.....	65
5.5	The Limits of Three-photon Through-skull Calcium Imaging.....	67
5.6	Conclusions .....	73
	APPENDIX A: MONTE CARLO SIMULATION FOR TISSUE TEMPERATURE RISE BY THREE-PHOTON MICROSCOPY .....	75
	APPENDIX B: MEASUREMENT OF OPTICAL POWER ABSORPTION BY IMMERSION WATER .....	86
	APPENDIX C: PROTOCOLS OF MOUSE BRAIN IMAGING THROUGH CRANIAL WINDOWS.....	88
	APPENDIX D: PROTOCOL FOR SKULL PREPARATION FOR CHRONIC IMAGING .....	90
	<b>REFERENCES .....</b>	<b>93</b>

## LIST OF FIGURES

Figure 1. Summary of Grey Matter Optical Properties in Literatures from 200 to 2000-nm Wavelength.....	8
Figure 2. The Schematic of 1320-nm 3PM and Characterization of the Laser .....	11
Figure 3. Characterization of 1300-nm Three-photon Microscope.....	13
Figure 4. Raw Calcium Recording Traces Plotted in Photon Counts .....	19
Figure 5. Schematic of Time Division Multiplexing for Simultaneous 2PM and 3PM Imaging.....	22
Figure 6. Simultaneous Calcium Imaging with 2PM and 3PM.....	24
Figure 7. Comparison of 1320-nm and 920-nm excitation attenuation and signal excitation efficiency in the mouse brain.....	26
Figure 8. Comparison of SBR for 1320-nm 3PM and 920-nm 2PM in the mouse brain. ....	32
Figure 9. 3PM Imaging of Neuronal Structure and Function in the SP Layer of the Mouse Hippocampus .....	41
Figure 10. 3PM Imaging of Spontaneous Activity in GCaMP6s-labeled Neurons in the SP Layer of the Mouse Hippocampus .....	44
Figure 11. Spontaneous Activity Traces of the Hippocampal Neurons Shown in Figure 10 .....	46
Figure 12. Continued Recording of Spontaneous Activities from the Same Hippocampal Neurons in Figure 10 .....	47
Figure 13. Revisit of the Same Neuronal Population in the SP Layer of the	

Hippocampus after One Week.....	49
Figure 14. Spontaneous Activity Traces of the Hippocampal Neurons Shown in Figure 13 .....	50
Figure 15. Comparison of Through-skull Vasculature Imaging by 3PM and 2PM. ....	55
Figure 16. Tissue Attenuation Length vs Excitation Pulse Duration. ....	60
Figure 17. Through-skull Imaging of Neural Structure and Function.....	62
Figure 18 Longitudinal Through-skull Neuronal Activity Recording at the Same Locations in an Awake Animal over a Period of 4 Weeks.....	65
Figure 19 Raw Data of Through-skull Neuronal Activity Traces .....	68
Figure 20. Through-skull Neuronal Activity Recording in an Awake Animal in Deeper Cortex .....	70
Figure 21. Immunolabeled Coronal Sections of Mouse Brains After Through-skull Imaging at 1320 nm.....	72
Figure 22. Monte Carlo Simulation Results of Light Intensity and Temperature Distribution in the Cortex.....	78
Figure 23. Prediction and Interpretation of the Critical Power for Tissue Temperature Rise.....	82
Figure 24. Light Attenuation with Immersion Water Thickness.....	86
Figure 25. Visual Examination of the Skull Transparency after the Skull Preparation. ....	92

## LIST OF TABLES

Table 1. Two- and three-photon Action Cross Sections of Fluorescein and GCaMP6f .....	30
Table 2. Two- and three-photon Excitation Parameters.....	31
Table 3. Optical Parameters of Grey Matter .....	76
Table 4. Derived Optical Parameters of Grey Matter.....	76
Table 5. Percentages of Excitation Photons for Different Destinations.....	80
Table 6. Thermal and Mechanical Properties of Grey Matter <sup>62</sup> .....	81

## CHAPTER 1

### 1 INTRODUCTION

#### ***1.1 Multi-photon Microscopy***

Since the first demonstration in 1990<sup>1</sup>, Multiphoton Microscopy (MPM) has found major applications in deep tissue imaging, owing to its unique optical sectioning ability in scattering media<sup>2</sup>. Light scattering and aberration in tissues is a fundamental challenge for any high resolution optical imaging technology to achieve greater depth *in vivo*<sup>3</sup>. In particular, the resolution and contrast of images are compromised as the result of wavefront distortion of the propagating light field, which is caused by the inhomogeneous and often dynamical distribution of refractive index<sup>4</sup>. The inefficiency of radiation transportation requires the input photons to increase exponentially with imaging depth to ensure that a small population of ballistic photons remain unscattered throughout the entire propagation<sup>2,5</sup>. For deep tissue imaging, the high imaging power ensued can eventually cause phototoxicity to the cells and heating of the tissue.

In the context of fluorescence microscopy, the total fluorescence can be separated into two parts: the fluorescence within the focal volume (i.e., the signal) and the fluorescence outside the focal volume (i.e., the background). In the case of one-photon excitation (1PE) of fluorescence, the background overwhelms the signal when the majority of fluorescence is excited by background photons. Moreover, when the signal and the background photons both have experienced multiple scattering, there is

no practical way to distinguish them. For example, a confocal pinhole can no longer effectively reject background photons, since the scattered background photons vastly outnumber ballistic signal photons, and have a fair chance of passing the confocal pinhole after enough randomization by scattering. MPM is relatively insensitive to light scattering by confining fluorescence excitation only to the focus with multi-photon excitation (MPE), where fluorescence emission (F) depends nonlinearly on excitation intensity (I):  $F \propto I^n$  ( $n \geq 2$ ). Since the nonlinearity strongly favors fluorescence excitation at the focus over the out-of-focus regions, 3D resolution can be obtained even in turbid media.

Another important advantage of MPM is the reduced scattering at the longer excitation wavelengths. In MPE, each photon carries a fraction of the energy required for fluorophore excitation, and therefore its wavelength is approximately a multiple of that for 1PE. Since tissue scattering is reduced with increasing wavelength at the visible and near-infrared spectral region<sup>6</sup>, the longer excitation wavelength allows a greater imaging depth (more quantitative discussion of tissue optical properties is presented in Section 1.4). Besides effectively extending imaging depth, long excitation wavelength (>1000 nm) also benefits imaging by lower generation of endogenous fluorescence in different tissues<sup>7,8</sup>.

The benefits of MPE also come with corresponding drawbacks. For example, MPE cross section is small. 2PE requires  $10^8$  to  $10^9$  times of peak excitation intensity as 1PE to achieve the practical signal strength for imaging, which demands the use of more expensive and powerful excitation sources such as ultrafast lasers. The longer wavelength in infrared also suffers from higher absorption by water, which in turn

limits the maximum allowable imaging power.

## 1.2 *Three-photon Microscopy*

The discussion in the previous section explains the general advantages of MPM over one-photon microscopy. In fact, both benefits and drawbacks of nonlinear microscopy are more accentuated in three-photon microscopy (3PM): The higher order of three-photon excitation (3PE) leads to even stronger optical sectioning but also even smaller cross section. The longer excitation wavelength further reduces scattering but causes more water absorption.

The investigation on the practicability of 3PM for *in vivo* imaging was motivated by the limitation of 2PM. In densely labeled samples, the imaging depth of 2PM is typically limited by high background fluorescence. Although 2PE can effectively reduce out-of-focus excitation, the background eventually becomes comparable to the signal since the total power grows exponentially with imaging depth. When the signal-to-background ratio (SBR) decreases to approximately one, the image suffers from low contrast and high background shot-noise, which makes it hard to extract spatial and temporal features. In densely labeled mouse cortex, 2PM with 925-nm excitation reached the SBR limit at around 850  $\mu\text{m}^9$ .

3PM has been shown to achieve greater imaging depth than 2PM using the same fluorescent dyes. 1700-nm 3PM is able to resolve vascular and neuronal structure through the entire cortex and under the highly scattering white matter in the mouse brain, at the maximum depth of  $\sim 1.3 \text{ mm}^{10}$  (1.6 mm for unpublished results).

To further expand the utility of 3PM, functional imaging was pursued. With

1300-nm 3PM, we have demonstrated activity imaging of GCaMP6s labeled neurons in the mouse hippocampus (Section 4)<sup>11</sup>, which can only be achieved by 2PM with the neo-cortex removed<sup>12,13</sup>. By rigorous comparison to 2PM, we have also shown that 3PM is more suitable for deep tissue imaging in densely labeled samples, with more power-efficient signal generation and superior SBR (Section 3). Furthermore, we have found an interesting application of 3PM for calcium imaging through intact mouse skulls, where the higher order nonlinearity helps to overcome aberration in the turbid layer (Section 5). We have successfully demonstrated 3PM applications where its benefits outweigh disadvantages, and it offers new capacities for *in vivo* calcium imaging in various samples.

Analogous to the history of 2PM, the successful demonstration of 3PM imaging, to a large extent, relied on the advancement of ultrafast lasers. The challenges for the excitation sources were: (1) selection of the optimal wavelengths with maximum 3PE efficiency and tissue transmission, and (2) high pulse energy required for deep imaging (>100 nJ on sample surface). Although 1550-nm high-power, turnkey fiber lasers were commercially available and could be used for 3PE of most red dyes, the high absorption by water at 1550 nm (Section 1.4) limits the maximum imaging power as well as depth. The first demonstration of 3PM deep tissue imaging utilized the 1700-nm excitation window, which was obtained by soliton self-frequency shift in a large core area photonic-crystal rod pumped by 1550-nm pulses<sup>10</sup>. The beauty of the method is that the large core area of the rod not only allows high pulse energy but also compresses pulse duration by soliton compression<sup>14</sup>. The broadened spectrum and increased peak intensity is essential for the frequency shift<sup>15</sup>. The development of the

1300-nm excitation sources took a completely different route: 1300-nm was generated by difference frequency generation in an optical parametric amplifier pumped by 1040-nm pulses (system details in Section 2.1). The major difficulty was the low wavelength conversion efficiency in free space crystals with limited coherence length. This was ultimately overcome by the powerful commercial lasers operating at 1040 nm, with as high as 40  $\mu$ J pulse energy at multi-MHz repetition rate (e.g. Spirit HE, Spectra Physics Inc.).

### **1.3 Calcium Imaging**

Rapid intracellular calcium change has long been associated with neuronal activities<sup>16,17</sup>. In particular, action potentials are always accompanied by transient calcium concentration surges, which play an important role in the regulation of neurotransmitter release at synapses<sup>18</sup>. The intracellular calcium concentration can be measured non-invasively with fluorescent calcium indicators, the brightness of which change when bound to calcium ions<sup>18</sup>. Protein-based genetically encoded calcium indicators (GECI) are especially versatile, since they can be introduced by genetic editing of transgenic animals, and allow labeling of specific cell types with expression throughout the entire nervous system<sup>18</sup>.

The combination of 2PM and GECI has been a powerful method for *in vivo* neurophysiological recordings. In the mouse brain, 2PM has enabled simultaneous activity recording of up to thousands of cortical neurons at single cell resolution, unparalleled by any other technology at the moment<sup>19</sup>.

Although 2PM calcium imaging had been demonstrated in the deep cortex by staining only one layer of neurons with red-shifted calcium indicators<sup>20</sup>, 3PM provides a unique solution to volumetric imaging of the entire densely labeled cortex, without requiring sparse labeling or suffering low SBR.

The major challenge for 3PM calcium imaging is temporal resolution, which is ultimately decided by signal strength. Calcium indicators usually have time constants around 1 s<sup>18</sup>, and 2PM calcium imaging is commonly performed with ~ 10-30 Hz recording frame rate<sup>19</sup>. For deep tissue structural imaging, 3PM had relied on low repetition rate and high peak power to maximize signal generation, which also led to low frame rate. Thanks to the development of GCaMP6 family<sup>21</sup> and transgenic animal lines with strong expression<sup>22</sup>, 3PM can be performed at sufficiently high repetition rate and temporal resolution. In fact, GCaMP6 family is currently still among the brightest and most widely used GECIs (e.g. GCaMP6s is 2.5x brighter than red-shifted GECI<sup>23</sup>). The new generation of jGCaMP7 developed by Loren Looger et al is even multiple times brighter). As a result, the combination of 1300-nm 3PM and GCaMP6s has found immediate applications in biological studies that was once experimentally impractical, such as volumetric mapping of neuronal activities in the entire visual cortex of mouse (on-going collaboration, unpublished).

#### ***1.4 Optical Properties of the Brain Tissue***

The selection of 3PE wavelength depends not only on the fluorescent dyes, but also on the tissue scattering and absorption properties in order to achieve maximal penetration with minimal phototoxicity.

Tissue optical properties can be most concisely captured by the following parameters: refractive index ( $n$ ), absorption ( $\mu_a$ ), scattering coefficients ( $\mu_s$ ), and scattering anisotropy factor ( $g$ )<sup>6</sup>.  $1/\mu_a$  can be interpreted as the travel distance by which 1/e of the photon population is absorbed by the tissue.  $1/\mu_s$  can be interpreted as the travel distance by which 1/e of the photon population experienced at least one scattering event. The anisotropy factor  $g$  is defined as the ensemble average of the scattering angle<sup>24</sup>.

Due to tissue scattering and absorption, ballistic photons decay exponentially with imaging depth, scaled by the effective attenuation length (EAL)  $l_e$  for every 1/e attenuation<sup>10</sup>. Given the same imaging power, a longer EAL indicates a proportionally larger imaging depth, since the image is formed by ballistic photons. Therefore, the normalized depth, defined as the physical depth divided by  $l_e$ , should be used for fair comparison of imaging depths in different samples or by different imaging modalities. Incidentally, EAL can be simply calculated from the scattering and absorption lengths, according to  $l_e = 1/(\mu_a + \mu_s)$ <sup>10</sup>.

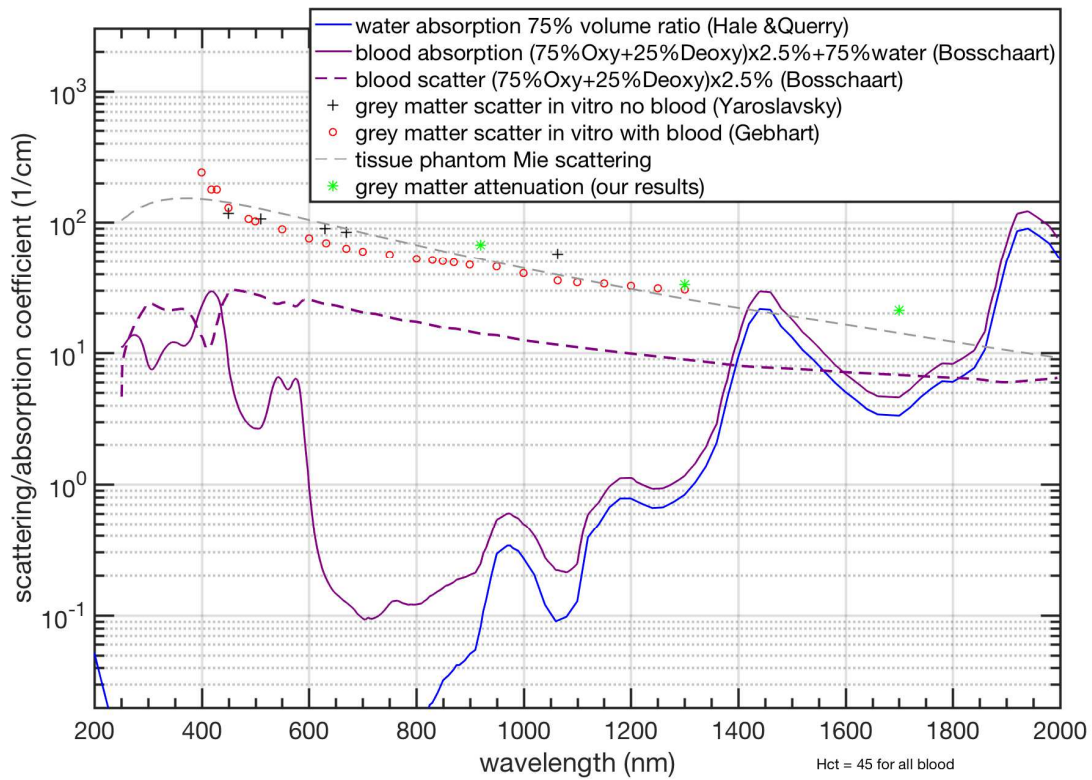


Figure 1. Summary of Grey Matter Optical Properties in Literatures from 200 to 2000-nm Wavelength

The blood is assumed to be composed of 75% in oxygenated and 25% deoxygenated form, with 2.5% volumetric fraction in the cortex<sup>5</sup>. The Mie scattering model utilizes the same parameters as in ref. 10 (water refractive index 1.33; scatterer refractive index 1.57, diameter 1  $\mu\text{m}$ , and volume fraction 0.0028). Our measurement on attenuation length in the mouse cortex can be found in ref. 10 (1675 nm), ref. 7 (1280 nm), and in Section 3.3 (920 and 1320 nm). Other tissue measurement results can be found in refs. 25, 26, 27, and 28, according to the author last names listed in the figure legend.

Figure 1 shows several important characteristics for light propagation in the mouse cortex. Between 600-1200 nm, light attenuation is dominated by tissue scattering (tissue scattering > blood scattering >> blood absorption). Blood absorption is

dominated by water in the near infrared regime ( $>1000$  nm), and can no longer be ignored from the total attenuation for wavelength longer than 1200 nm (tissue scattering  $\sim$  blood absorption  $\sim$  water absorption  $\sim$  blood scattering). 1300 nm and 1700 nm hit the respective local minima of water/blood absorption, and thus are suitable windows for 3PM imaging. Overall, 1700 nm has longer EAL than 1300 nm, but has higher absorption as well.

### ***1.5 Considerations on Deep Tissue Imaging***

The imaging depth for 3PM *in vivo* can be ultimately limited by overwhelming background and/or thermal damage induced by high average power.

The SBR limit of 2PM is approximately 4 attenuation lengths in densely labeled mouse cortex<sup>31</sup>. Although 3PM is able to extend this limit by suppressing background fluorescence with the higher order nonlinear excitation<sup>10</sup>, the signal may still diminish through the deterioration of the point spread function (PSF) at extreme imaging depth, especially in light of the fact that 3PE signal is more susceptible to aberration than 2PE<sup>32</sup>. Therefore, the actual experimental results may deviate from theoretical prediction, and wavefront shaping methods become necessary to restore diffraction limited focus at large imaging depth.

Laser-induced tissue damage can be categorized into thermal and nonlinear damage. For 3PM imaging in shallow tissue, nonlinear damage at the focus by high excitation peak intensity happens before any significant heating of the tissue. As imaging depth increases, thermal damage eventually limits the maximum power as well as imaging depth achievable by 3PM, as the total power grows exponentially with

depth.

The thermal damage threshold is expected to be lower for 3PM than 2PM, due to the higher water absorption in the infrared regime (Figure 1). In order to extend 3PM imaging depth, the repetition rate has to be reduced at the expense of field-of-view (FOV) or frame rate. As a result, for each imaging depth, an optimal repetition rate exists that maximizes FOV at a given frame rate, while still keeps the average and peak power low enough to avoid damage. The determination of such repetition rate necessitates the characterization performed in Section 3.

## CHAPTER 2

### 2 THE METHODOLOGY OF THREE-PHOTON CALCIUM IMAGING

This chapter covers the principles of three-photon calcium imaging and the basic experimental setup. Most results in chapter 2-5 were derived from the same setup, unless additional modification is stated.

#### 2.1 Excitation Sources and Microscope Setup

##### 2.1.1 Excitation Sources

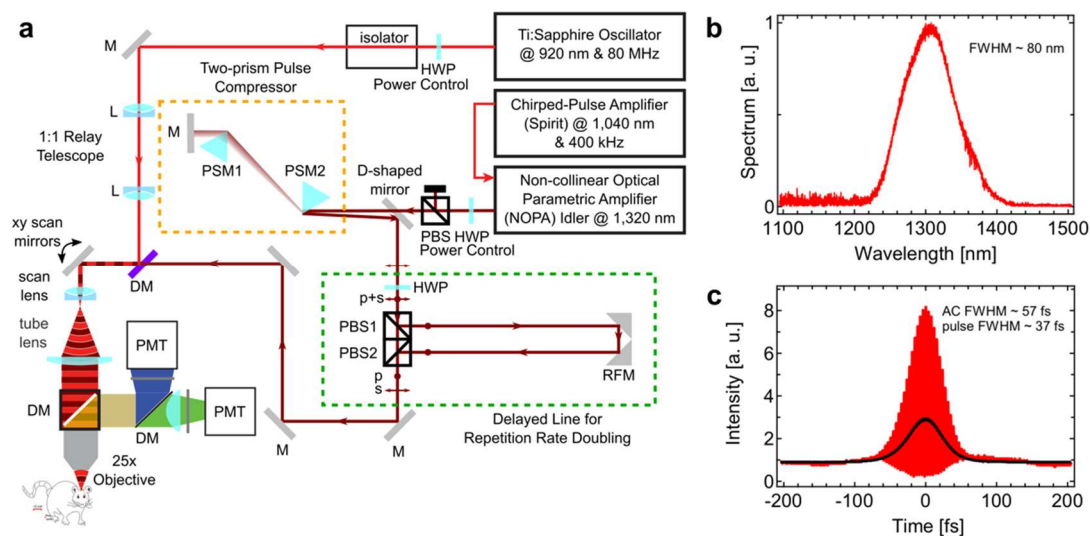


Figure 2. The Schematic of 1320-nm 3PM and Characterization of the Laser

**a**, Schematic of home-built microscope for two- and three-photon imaging.

In the delay line, the p and s polarization are relative to the beam splitting surfaces of PBS1 and PBS2. M: mirror; L: lens; HWP: half-wave plate; PBS: polarizing beam-splitter cube; PSM: prism; RFM: 90-degree roof mirror; DM: dichroic mirror; PMT: photomultiplier tube.

**b**, Measured NOPA output spectrum centered around 1320 nm.

c, Measured interferometric (red) and intensity (black) second-order autocorrelation trace of the pulse at the objective focus, with dispersion pre-compensation.

The excitation source for 1320-nm 3PM is a non-collinear optical parametric amplifier (NOPA, Spectra Physics) pumped by a regenerative amplifier (Spirit, Spectra Physics). A two-prism (SF11 glass) compressor is used to compensate for the normal dispersion of the optics of the light source and the microscope, including the objective. The NOPA operates at wavelength centered at 1320 nm, and provides an average power of  $\sim 700$  mW (1750 nJ per pulse at 400 kHz repetition rate). The pulse duration (measured by second-order interferometric autocorrelation) under the objective is  $\sim 37$  fs after optimizing the prism compressor distance.

An optical delay line is used to double the laser repetition rate to 800 kHz, by splitting each excitation pulse into a pair of equal power with  $\sim 10$  ns delay between them, which is much longer than the green fluorescent protein fluorescence lifetime<sup>25</sup>. The purpose of the delay line is to double the signal strength without increasing peak excitation intensity, which may cause nonlinear damage or fluorophore saturation.

The excitation source for 2PM is a mode-locked Ti:Sapphire laser (Tsunami, Spectra Physics) centered at 920 nm. The 920-nm beam and 1300-nm beam are spatially overlapped and directed to the same microscope, and then combined by a dichroic mirror. For simultaneous 2PM and 3PM imaging, an electro-optic modulator (EOM) was placed in 920-nm beam path for time-division multiplex of the two wavelengths (detailed in Section 3.1). An 1:1 telescope with variable distance between the lenses (Figure 2) is added in 920-nm beam path to allow fine-adjustment of axial

depth of 920-nm focus after the objective in order to align with the 1320-nm focus.

The excitation source for 1700-nm 3PM was solitons centered at 1700 nm generated by soliton self-frequency shift in a photonic crystal fiber pumped by a fiber laser at 1550 nm. The excitation source and the microscope are described in more detail in ref. <sup>10</sup>.

### 2.1.2 Microscope

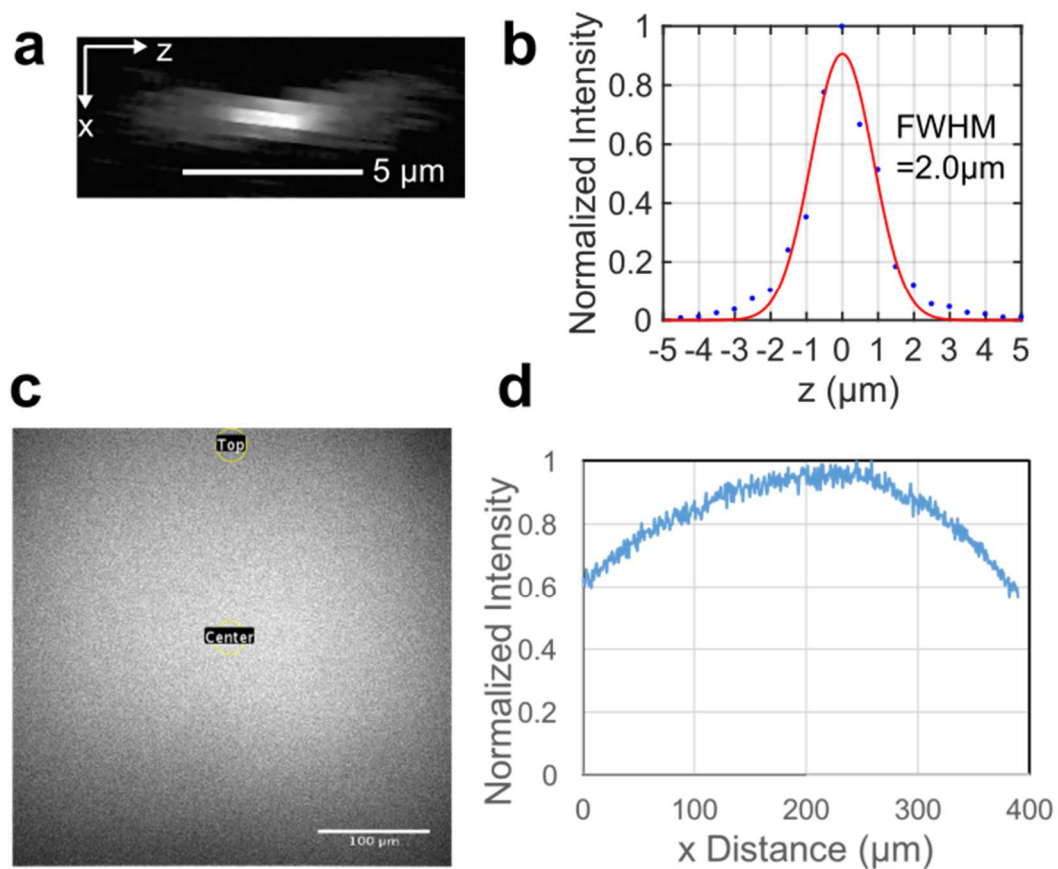


Figure 3. Characterization of 1300-nm Three-photon Microscope

**a**, Maximum intensity projection on xz plane of 1320-nm 3PM point spread function (PSF) measurement using a 0.5 μm diameter fluorescent bead on a glass slide. Scale bar, 5 μm.

**b**, Intensity profile along the z axis of the PSF in **(a)** normalized to its maximum value, and then fitted with a Gaussian profile. The intensity is integrated in each lateral (xy) plane.

**c**, Measurement of the uniformity of 3PE signal across the FOV in fluorescein solution ( $\sim 40 \mu\text{M}$ ,  $\text{pH} \sim 10$ ). Scale bar,  $100 \mu\text{m}$ .

**d**, Intensity profile along the horizontal axis (fast scanning axis) of the FOV in **(c)**.

The images are taken with a custom-built multiphoton microscope (Figure 2) with a high-numerical aperture objective (Olympus XLPLN25XWMP2, 25X, NA 1.05). The objective is under-filled to reduce unnecessary loss of power in the marginal rays, and the  $1/e^2$  beam diameter of the excitation beam is  $\sim 11 \text{ mm}$ , which is  $\sim 70\%$  of the objective back aperture diameter (calculated as twice of the product of focal length and NA;  $7.2 \text{ mm} \times 1.05 \times 2 = 15.12 \text{ mm}$ ). The resolution of the microscope was measured on  $0.5\text{-}\mu\text{m}$  diameter fluorescent beads on glass slides (Fluoresbrite, YG Microspheres, Polysciences, Inc.), and the axial FWHM was  $2 \mu\text{m}$  (Figure 3a and b).

A galvo-galvo XY scanning mirror pair (6210H, 5 mm diameter for the fast scanning mirror, Cambridge Technology) is used for imaging acquisition, and the mid-point of the mirrors is conjugated to the objective back aperture (coincident with the back focal plane, which measures  $\sim 40 \text{ mm}$  from the objective thread shoulder towards the front window) by a scan and tube lens pair (detailed in the next paragraph). The maximum line rate is  $0.5 \text{ ms/line}$  for bidirectional scanning. A typical configuration for neuronal activity recording is  $256 \times 256$  pixels/frame at  $8.49 \text{ Hz}$  frame rate.

The scan lens and the tube lens used in the microscope are achromatic (AC-254-

040-B, Thorlabs Inc.) and plano-convex lens (LA 1399-C, Thorlabs Inc.), respectively. The tube and scan lens form a telescope with a beam size magnification of 4.375x (175 mm/40 mm = 4.375). The uniformity of the scanning field of view was measured by 3PE of fluorescein dye pool solution ( $\sim 40 \mu\text{M}$ , pH  $\sim 10$ ), and the 80% fall-off FOV was measured to be  $\sim 250 \mu\text{m}$  (Figure 3c and d).

The signal is epi-collected through the objective and then reflected by a dichroic beam splitter (FF705-Di01-25x36, Semrock) to the detection system. There are two detection channels: one for fluorescence signal and the other for third harmonic generation (THG). For GCaMP6s imaging, we used a photomultiplier tube (PMT) with GaAsP photocathode (H7422-40, Hamamatsu) for the fluorescent signal and an ultra bialkali PMT (R7600-200, Hamamatsu) for the THG signal. A 488-nm dichroic beam splitter (Di02-R488-25x36, Semrock) is inserted at 45 degrees to the signal beam path to separate and direct fluorescence and THG to their respective PMTs. Fluorescence generated by fluorescein and GCaMP6s is selected by a  $520\pm 30$  nm band-pass filter (Semrock), and THG around 440 nm is selected by a  $435\pm 20$  nm filter (Semrock). When imaging Alexa 680, a GaAs PMT (H7422-50, Hamamatsu) is used instead for the fluorescence channel, which has higher sensitivity at longer wavelength. Meanwhile, the fluorescence filter is changed to  $716\pm 20$  nm (Semrock) filter to pass Alexa 680 fluorescence while blocking the second harmonic of 1320 nm.

For signal sampling, the PMT current is converted to voltage by a transimpedance amplifier with 10MHz bandwidth (C9999, Hamamatsu), providing adequate temporal resolution for photon counting. For analog signal acquisition, an additional 1.9 MHz low pass filter (Minicircuits, BLP-1.9+) is used before digital sampling. Analog-to-

digital conversion is performed by a data acquisition card (NI PCI-6115, National Instruments). The signal acquisition system displays shot-noise limited performance (Section 2.2), and light shielding is carefully done to achieve dark counts of 20-40 photons per second under actual imaging conditions without laser scanning. ScanImage 3.8 running on MATLAB (MathWorks) is used for image acquisition and control of a 3D translation stage to move the sample (M-285, Sutter Instrument Company). All imaging depths and thickness are reported in raw axial movement of the motorized stage, unless otherwise stated. The refractive indices of skull and brain tissue (1.55 for the bone and 1.35 to 1.37 for the cortex<sup>33</sup>) are higher than that of water (1.32), which result in slight under-estimate of the actual depth in the experiments (~ 12% for the skull thickness and ~3% for the depth in the brain tissue).

### 2.1.3 Imaging Configuration and Analysis

Imaging acquisition are controlled by ScanImage 3.8 running on MATLAB. High resolution structural images are typically taken with 512x512 pixels/frame, at 0.5 Hz frame rate, with multiple frame averages at each depth. Neuronal activities are recorded using 256x256 pixels/frame at 8.49 Hz frame rate. For simultaneously 2PM and 3PM (detailed in Section 3.1), calcium activities are recorded using 4096x80 pixels with 13.6 Hz frame rate. Photomultiplier tube offset voltage is subtracted all cases.

For structural imaging, multiple frames at the same depth are averaged in reduce noise. For activity imaging, mechanical drift in the original image frames, if any, is corrected by TurboReg plug-in in ImageJ. Regions of interest (ROIs) are generated by

manual segmentation of neuron bodies. The average pixel values and areas of ROIs are then exported to MATLAB 2016b for further processing.

For normalized calcium traces, fluorescence intensity traces are low-pass filtered with a hamming window of a preset time constant (different in different cases). Spikes are inferred simply by taking local maxima in the traces. Baselines of the traces ( $F_0$ ) are determined by excluding spikes as well as their rising and falling edges. Traces ( $F$ ) are normalized according to the formula  $(F - F_0)/F_0$ .

## ***2.2 Shot-noise limited Microscope Performance and Quantification of Photon Counts from Images***

The noise of single-photon-sensitive detectors, such as photomultiplier tubes, is bounded by shot noise. To achieve the best fidelity of measurement, the system should be carefully characterized and tuned to approach shot-noise limited performance.

The microscope was tested for shot-noise limited performance by photon counting the fluorescence excited by parking 1320-nm or 920-nm focus in fluorescein solution ( $\sim 40 \mu\text{M}$  and  $\text{pH}=10$ ). The laser power was chosen ( $\sim 0.3 \text{ mW}$  for both wavelengths) to ensure the photon counts per second is lower than 5% of the laser repetition rate, which limits the photon stacking error to within 2.5% of the total counts. According to Poisson statistics, the fraction of underestimation by photon stacking error is  $1 - (1 - e^{-\lambda})/\lambda$ , where  $\lambda$  is the average counts per second divided by the laser repetition rate. For photon-counting experiments, the PMT anode current from Hamamatsu H7422-40 was first amplified with a 10 MHz bandwidth pre-amplifier (C9999, Hamamatsu), and then fed to a photon counter (SR400, Stanford

Research). Counts were taken at 1 s intervals for multiple repeats, and the sample variance was calculated and compared to the average counts. Shot-noise limited performance was confirmed for the imaging system.

The pixel values in acquired images can be converted to photon counts by a conversion factor calibrated in the following way. A 920-nm or 1320-nm focus was parked in the fluorescein solution, and then photon counting and imaging were performed sequentially. The linearity between the average pixel values and photon counts were tested by changing the laser power, and the ratio between them were used as the conversion factor. The conversion factor was further confirmed by observing the first mode in a pixel value histogram. The zeroth mode of the histogram peaks at the PMT offset voltage, and the first mode to the right of it equals the pixel value corresponding to exactly one photon. Higher order modes can also be observed representing pixels receiving integer multiple of photons. Furthermore, at 5 MHz digital sampling rate (i.e. 5 million pixels per second), voltage pulses corresponding to individual photons can be resolved and photon counting could be performed directly on acquired images, which is consistent with analog photon counting.

Despite the possibility of registering images in the unit of photon counts, analog voltage signal is still preferred for image acquisition, since it reduces photon stacking error at high photon counts. When multiple photons excited by the same excitation pulse arrive at the PMT, the time separation between them is only several nanoseconds so that individual pulses cannot be distinguished by either analog or digital photon counting. In the case of voltage signal, voltage pulse generated by each stacked photon superimpose on each other to form a single pulse of higher amplitude, which can be

faithful registered.

### 2.3 Calculation of the Minimum Signal for Spike Detection based on the Characteristics of the Calcium Indicator

Compared to structural imaging, the major challenge of functional imaging is the much higher temporal resolution required to capture dynamics. Structural imaging can be performed with an integration time from seconds to hours, as long as the sample stays stationary. On the other hand, calcium imaging usually requires about 10 Hz frame rate or higher. Therefore, the minimum requirement on the signal strength for functional imaging can be one or two orders of magnitude as structural imaging. In this section, the minimum signal strength required for faithful detection of GCaMP6s spikes is calculated.

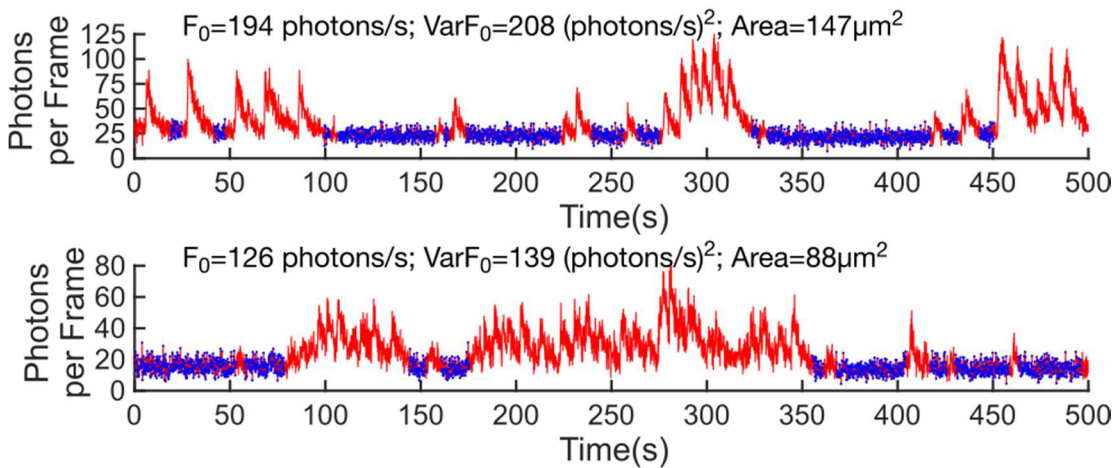


Figure 4. Raw Calcium Recording Traces Plotted in Photon Counts

Two raw activity traces of hippocampal neurons recorded at 8.49 Hz frame rate in unit of photon counts per frame. Blue dots indicate the baseline, based on which the average baseline photon counts per second ( $F_0$ ) and the

baseline variance ( $\text{Var}F_0$ ) were calculated.

High quality calcium imaging enables reliable detection of calcium transients in presence of noise. A calcium spike in the fluorescent intensity trace can be modeled by an exponential decay function using the decay time for the calcium indicator. In the absence of artifacts such as sample motion, deviation from the model results from the noise in the photon detection and data acquisition system. With a photomultiplier tube as the fluorescence detector and careful light and electronic noise shielding, as in our system, the calcium imaging noise is dominated by photon shot noise. Therefore, quantifying the fluorescence signal in the unit of photon counts, instead of analog voltage or pixel value, enables us to estimate the total noise level. In a shot-noise limited imaging system, the noise (N) and the signal (S) obey the relation:  $N = \sqrt{S}$ , both measured in the unit of photon counts per second. When the signal-to-noise ratio (SNR) becomes high enough, calcium spikes can be detected with high confidence. In fact, the minimum photon counts required for a single spike detection can be calculated at a given confidence level. According to the model by Wilt et al<sup>34</sup>, a single discriminability index ( $d'$ ), as defined by Equation (1), is used to assess the quality of measurement:

$$d' \approx \frac{\Delta F}{F} \sqrt{\frac{F_0 \tau}{2}} \quad (1)$$

where  $\tau$  is decay time,  $\Delta F/F$  is the peak fluorescence change induced by a single action potential, and  $F_0$  is the baseline fluorescence signal in the ROI, such as a cell body.

Using the parameters for GCaMP6s ( $\Delta F/F \sim 30\%$ ,  $\tau \sim 2\text{s}$ <sup>21</sup>,  $F_0$  needs to be  $\sim 100$

photons/second to achieve  $d' = 3$ . A higher  $d'$  value corresponds to better detection accuracy, and  $d' = 3$  gives 93% true detection and 7% false detection rate. If  $d' \sim 3$  is used as the criteria for acceptable recording quality, the above calculation establishes the minimum signal level needed to detect a single action potential. For a calcium transient induced by a short burst of action potentials, the apparent  $\Delta F/F$  is the accumulation of the single action potentials. Therefore, the  $F_0$  required for detection can be significantly lower because of the larger  $\Delta F/F$ .

In Figure 4, we show examples of calcium traces recorded from GCaMP6s-labeled hippocampal neurons using 3PM. ROIs were generated by manual segmentation of neuron bodies. The raw fluorescent intensity trace was generated by summing all the pixels in the ROI and then converting to photon counts. Spikes were inferred by thresholding the Poisson-distribution-based likelihood function<sup>34</sup> derived from each trace (the discrimination threshold used is  $C = \ln((1-r)/r)$ , where  $r$  is the estimated firing rate. The initial firing rate was estimated for each individual trace as the fraction of the trace that is more than 1.5 standard deviation above its mean, which in practice gives good results.). Baselines of the traces ( $F_0$ ) were then determined by excluding the spikes as well as their rising and falling edges. The shot-noise-limited imaging performance is confirmed by the equal variance and mean of the baseline photon counts. The baseline counts of both traces are above the threshold for single-spike detection (i.e. 100 photons per second), and therefore spikes of about 30%  $\Delta F/F$  can be resolved (at  $\sim 160$  s for the top trace, and  $\sim 55$  s for the bottom one). The first trace in Figure 4 has higher photon counts and thus better discriminability.

## CHAPTER 3

### 3 COMPARISON BETWEEN TWO-AND THREE-PHOTON CALCIUM IMAGING DEEP IN THE DENSELY LABELED MOUSE BRAIN

The performance of 1320-nm 3PM was quantified and compared to 920-nm 2PM for GCaMP6s calcium imaging in densely labeled mouse brain. Compared to 2PM, 3PM is significantly more suited for calcium imaging in deep cortex and beyond, with higher signal excitation efficiency and signal-to-background ratio. These advantages resulted from the reduced scattering at the longer excitation wavelength and the improved 3D confinement of 3PE. The thermal and nonlinear damage thresholds are estimated for 3PM imaging. Based on these results, a guideline on optimizing system parameters is proposed for 3PM applications.

#### 3.1 *Time-division Multiplexing for Simultaneous Two- and Three-photon Imaging*

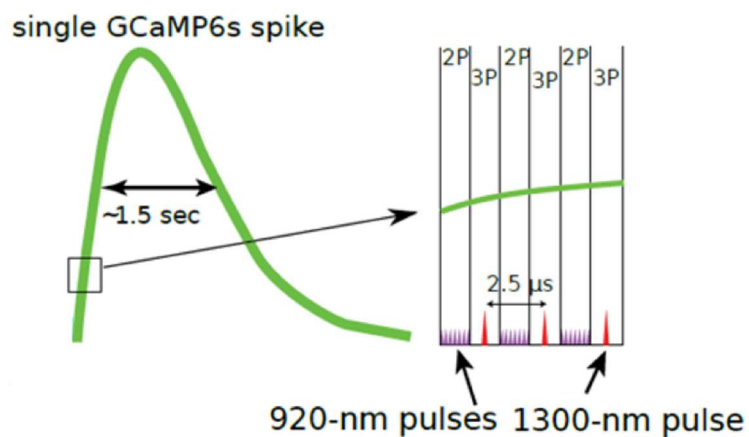


Figure 5. Schematic of Time Division Multiplexing for Simultaneous 2PM

## and 3PM Imaging

In order to obtain the most rigorous possible comparison between functional two- and three-photon imaging, the same neurons should be imaged by the two modalities preferably at the same time, due to the time-varying nature of neural activities and event-to-event uniqueness of calcium spikes. Therefore, a time division multiplexing (TDM) scheme was employed to allow almost simultaneous recording of calcium dynamics by 920-nm 2PM and 1320-nm 3PM.

The schematics of TDM are illustrated in Figure 5. The 920-nm beam was produced by a Ti:Sapphire laser and the 1320-nm beam by NOPA. The 920-nm and 1320-nm beams are first spatially overlapped to have the same focal position after the objective. During the imaging, the intensity of 920-nm beam is modulated with an electro-optic modulator (EOM). The EOM is driven by a radio frequency signal derived from the NOPA laser clock such that the 920-nm beam is only switched on in-between every two adjacent 1320-nm pulses, for  $\sim 1 \mu\text{s}$ . Therefore, the sample is alternatively illuminated either with 920-nm beam for 2PE or 1320-nm beam for 3PE. The two- and three-photon excited fluorescence signals are separated into 2 channels according to the 1320-nm laser clock (which is also recorded) with a post-processing MATLAB script.

### 3.2 Correlation between Two- and Three-photon Calcium Imaging Traces in the Shallow Cortex

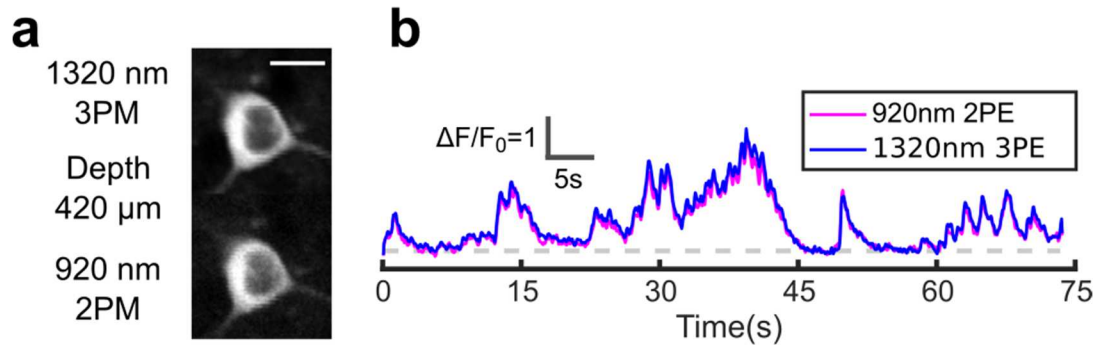


Figure 6. Simultaneous Calcium Imaging with 2PM and 3PM.

**a**, Images of a cortical L4 neuron, simultaneously recorded by 920-nm 2PM and 1320-nm 3PM.

**b**, The calcium trace of the neuron in (a), simultaneously recorded by 2PM and 3PM. Both traces were low-pass filtered with a hamming window of time constant 0.37 s. Perfect correlation and nearly the same spike amplitudes are observed from the traces.

The maximum 2PE cross section of the GCaMP6 family (in Ca-bound forms) lie in-between 920-980 nm<sup>23,35</sup>. Unpublished results indicate that the maximum 3PE cross section of GCaMP6f happens around 1320-1340 nm<sup>36</sup>, and therefore partially justifying the choice of the 3PE wavelength. However, since the wavelength dependence of 3PE cross section of GCaMP6f cannot be simply deduced from 2PE<sup>35,36</sup> (for both Ca-bound or Ca-unbound form of the protein), it should not be taken for granted that 3PE of the calcium indicator would achieve the same sensitivity to calcium concentrations or even produce similar calcium traces as 2PM. In order to

study the correlation between 3PM and 2PM derived calcium traces, we used TDM for simultaneous calcium activity recording with 1320-nm 3PM and 920-nm 2PM.

For shallow mouse cortical neurons in layer 2/3 and 4, we obtained essentially identical calcium traces with the 2PM and 3PM (Figure 6b and c), with a correlation factor of  $0.98 \pm 0.01$  (60 traces, each 75s on neurons located from 200 to 400  $\mu\text{m}$  in depth). Our data also show that  $\Delta F/F$  of GCaMP6s with 1320-nm 3PE is close to that of 920-nm 2PE, with the ratio  $(\Delta F/F)_{3P}/(\Delta F/F)_{2P} = 1.0 \pm 0.25$  (mean  $\pm$  standard deviation,  $n=904$  calcium spikes). The average 3PE  $\Delta F/F$  is  $131 \pm 99\%$  (mean  $\pm$  standard deviation), for all spikes with amplitude larger than 30%. The results indicate that, despite the distinct excitation mechanism (2PE vs 3PE), 3PM at 1320-nm excitation of GCaMP6s is able to achieve the same high signal strength and  $\Delta F/F$  as 2PM in the shallow mouse cortex.

### ***3.3 Effective Attenuation Length of 1320 nm and 920 nm in the Mouse Brain***

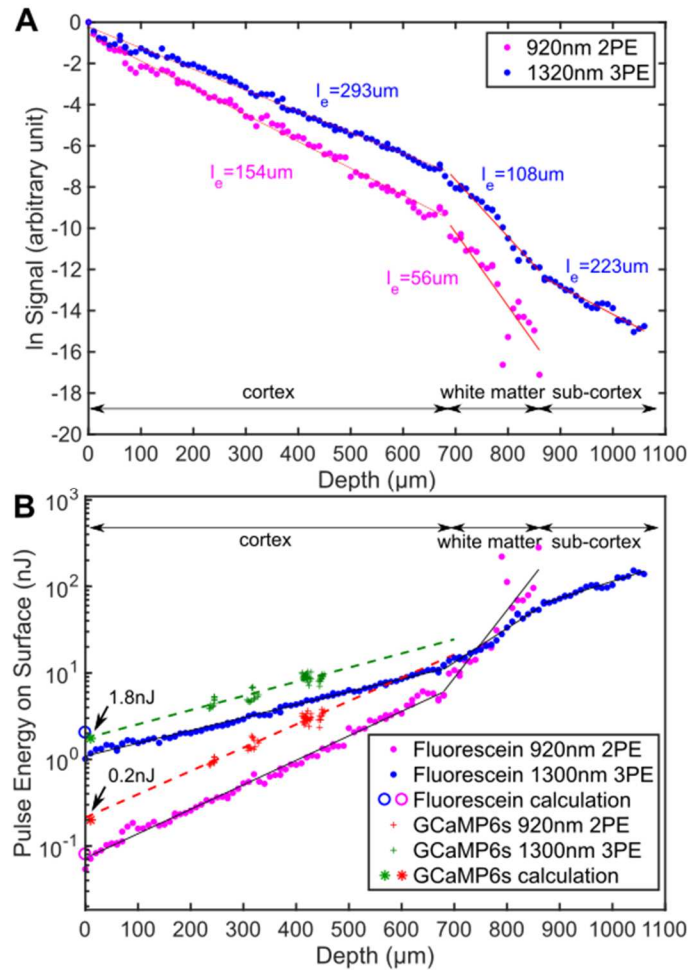


Figure 7. Comparison of 1320-nm and 920-nm excitation attenuation and signal excitation efficiency in the mouse brain

**a**, Semi-log plot of fluorescence signal vs imaging depth for fluorescein-labeled blood vessels. Each curve is normalized to its signal on the sample surface. The EALs derived from linear regressions are displayed next to the curves ( $n=2$ ,  $\sim 20$  weeks old, both produce similar results).

**b**, The required pulse energy on the brain surface as a function of imaging depth for generating 0.1 detected signal photon per pulse in fluorescein-labeled blood vessels (C57BL/6J, retro-orbital injection with 25 mg fluorescein dextran conjugate in 200  $\mu\text{l}$  saline, 70kDa molecular weight, invitrogen) and GCaMP6s-labeled neurons (*CamKII-tTA/tetO-GCaMP6s*,

n=3, 11-13 weeks old). The pulse duration is normalized to 60 fs for both curves.

In order to characterize the tissue attenuation difference between 1320-nm and 920-nm excitation, fluorescence signal decay as the function of imaging depth was measured. By imaging fluorescein labeled blood vessels within the same field-of-view of the mouse brain with 2PM and 3PM simultaneously, any sample-to-sample variations and sample fluctuations over time was eliminated. Since 2PE and 3PE of fluorescein have the identical emission spectrum and collection geometry, there was no difference in collection efficiency. Although 2PE and 3PE signal might be affected by aberration differently as the imaging depth increases<sup>32</sup>, the impact of mild aberration (which is the case in the brain cortex) is expected to be orders of magnitude smaller than the decay of the excitation intensity at the focus. Consequently, the ratio between 3PE and 2PE signal reflects mainly the difference in the attenuation of 1320-nm and 920-nm excitation. As shown in Figure 7a, the attenuation of the 3PE signal is about 1/9 of that of the 2PE signal at the depth of 700  $\mu\text{m}$  in the cortex, and almost 1/50 at the distal end of the white matter at 860  $\mu\text{m}$ . By fitting the signal vs depth with an exponential function, the EAL at 1320 nm in mouse cortex is almost twice that at 920 nm. Since the maximum imaging depth roughly scales with EAL, the longer EAL of 1320 nm poses a big advantage over 920 nm, which will be quantified in more details in the following sections.

### 3.4 *Signal Yield per Excitation Pulse on Fluorescein and GCaMP6s*

One direct implication of the longer EAL of 1320 nm is that 1320-nm 3PM may require less power on the brain surface than 920-nm 2PM, when imaging deep enough in the sample. In general, due to the small 3PE cross section, 3PE requires higher excitation pulse energy at the focus than 2PE in order to generate the same signal strength, given the same dye, concentration, pulse duration etc. For deep tissue imaging, however, excitation attenuation by the tissue reduces the excitation power at the focus drastically. In Figure 7b, we plotted the pulse energy at the brain surface for different imaging depths such that 0.1 photon is detected each excitation pulse. The plots are derived from the EAL data shown in Figure 7a, after re-normalization to 60 fs pulse duration for both 920-nm and 1320-nm pulses. Light absorption by the immersion water was taken into account when calculating the pulse energy for 1320 nm (APPENDIX B). To generate the same level of signals in fluorescein-labeled blood vessels on the brain surface, 3PE requires about 14 times the pulse energy of 2PE. As the imaging depth increases, the difference in pulse energy reduces and eventually 3PE becomes more power-efficient than 2PE at around 750  $\mu\text{m}$ , which is the cross-over depth. The same trend can be observed on GCaMP6s labeled neurons. At the brain surface, 3PE at 1320 nm requires  $\sim 9$  times the pulse energy of 2PE at 920 nm (1.8 nJ vs 0.2 nJ), while at the bottom of the cortical layers around 700  $\mu\text{m}$ , the pulse energy required for 3PE becomes comparable to that of 2PE. Our data show that, with the same repetition rate and pulse duration, 3PM can be more power-efficient than 2PM in terms of signal generation when imaging deep in the mouse brain.

The cross-over depth can also be estimated based on 2PE and 3PE action cross sections of fluorescein<sup>37</sup> and GCaMP6f<sup>35,36</sup>. As the first step, the ratio of the pulse energy required for 2PE and 3PE to obtain the same signal is calculated for imaging on the brain surface, and then the cross-over depth is calculated based on the measured EALs. For 2PE and 3PE, the detected signal photons per excitation pulse can be calculated by equation (2) and (3) respectively<sup>38,37</sup>:

$$\text{2PE signal photons per pulse} = \frac{1}{2} \frac{g_p^{(2)}}{\tau} \phi C (\eta \sigma_2) n_0 \frac{8E^2}{\pi \lambda} \quad (2)$$

$$\text{3PE signal photons per pulse} = \frac{1}{3} \frac{g_p^{(3)}}{\tau^2} \phi C (\eta \sigma_3) n_0 \frac{3.5(NA)^2 E^3}{\lambda^3} \quad (3)$$

Where  $g_p^{(n)}$  is the temporal coherence factor of a single Gaussian profiled pulse,  $\tau$  is the laser pulse width,  $\phi$  is the system collection efficiency,  $C$  is the concentration of the fluorophore,  $\eta \sigma_n$  is the n-photon excitation action cross section, and  $n_0$  is the refractive index of the medium,  $\lambda$  is the excitation wavelength in vacuum, NA is the numerical aperture, and  $E$  is single pulse energy. Given 0.1 photon detected per excitation pulse, the required pulse energy  $E$  was solved by plugging the values of the parameters in Table 1 and Table 2. Note that absolute system collection efficiency and fluorophore concentration were estimated, since they are hard to be precisely determined *in vivo*. The system collection efficiency was estimated to be 0.01: The collection efficiency of an objective lens of 1.05 NA is 20%, but reduces to 16% when imaging at one scattering length<sup>30</sup>. The rest of the collection system was estimated to be between 20-35% efficiency, since it is similar to the design in ref 39, except for a smaller aperture (25.4 mm vs 40 mm). Finally, Hamamatsu H7422-40 has a quantum

efficiency of ~ 40%, and the overall efficiency is the product of all the components. The fluorophore concentration was then estimated so that the 2PE pulse energy required for 0.1 photon detection on sample surface roughly match experimental results (Figure 7). As a result, the blood fluorescein concentration was estimated to be 3  $\mu\text{M}$ , and intracellular GCaMP6 concentration 0.4  $\mu\text{M}$ . Despite the estimation involved in calculation, the ratio of 3PE and 2PE pulse energy is relatively insensitive to the magnitude of fluorophore concentration or collection efficiency (e.g. a 64x underestimate of dye concentration leads to 2x of the ratio of 3PE to 2PE pulse energy).

For fluorescein, the ratio of 3PE to 2PE pulse energy is calculated to be 2 nJ/0.08 nJ = 25 times. For GCaMP6f, the ratio is 1.73 nJ/0.2 nJ = 8.7 times. Both ratios are quite close to actual measured values (14x for fluorescein, and 9x for GCaMP6s).

Table 1. Two- and three-photon Action Cross Sections of Fluorescein and GCaMP6f

	2PE cross section ( $\eta\sigma_2$ ) $10^{-50}\text{cm}^4 \text{ s/photons}$	3PE cross section ( $\eta\sigma_3$ ) $10^{-83} \text{cm}^6 (\text{s/photons})^2$
Fluorescein (pH=13)	26 at 920 nm <sup>38</sup>	1.6 at 1300 nm <sup>37</sup>
GCaMP6f	~33 at 920 nm <sup>35</sup>	~19 at 1320 nm <sup>36</sup>

Table 2. Two- and three-photon Excitation Parameters

	Numerical Aperture NA	Pulse Duration $\tau$ (fs)	$g_p^{(n)}$	Refractive Index $n_0$	Collection Efficiency $\phi$
920 nm 2PE	0.9 (under-filling)	60	0.51	1.36	0.01
1320 nm 3PE	0.9 (under-filling)	60	0.66	1.36	0.01

Based on the ratio of 3PE to 2PE pulse energy, the cross-over depth can be calculated by solving for  $z$  in equation (4). For example, with  $l_{e,1320nm} = 300 \mu\text{m}$ , and  $l_{e,920nm} = 150 \mu\text{m}$  (Figure 7), and the pulse energy ratio of 8.7, the cross-over depth  $z$  is solved to be  $650 \mu\text{m}$  in the cortex. If the ratio changes to 25, then cross-over depth is at  $965 \mu\text{m}$ , which is beyond the cortex.

$$\frac{\text{Focal 3PE pulse energy}}{\text{Focal 2PE pulse energy}} = \frac{\exp(-z/l_{e,1320nm})}{\exp(-z/l_{e,920nm})} \quad (4)$$

### 3.5 Comparison of Signal-to-background Ratio in Deep Cortex

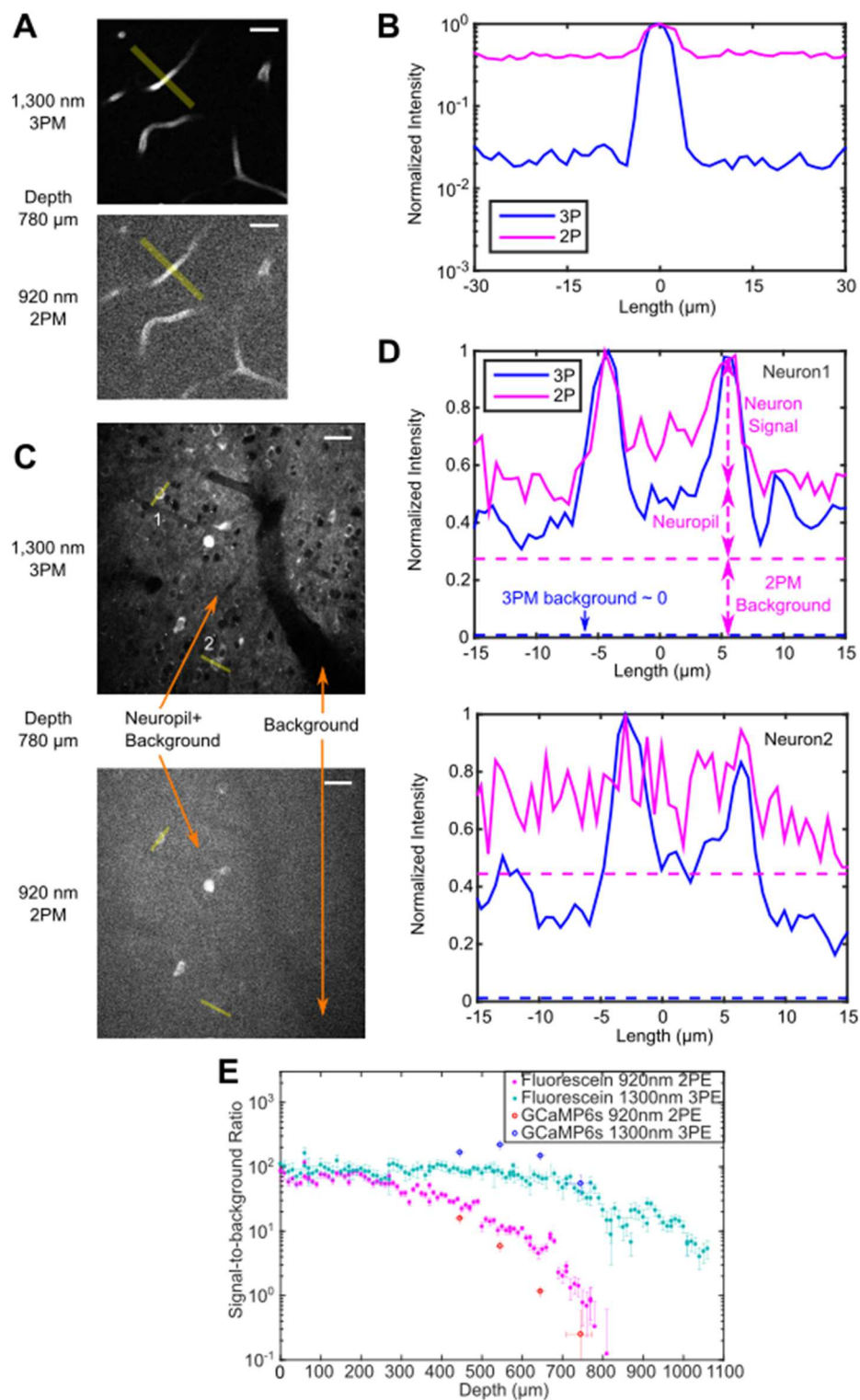


Figure 8. Comparison of SBR for 1320-nm 3PM and 920-nm 2PM in the

mouse brain.

**a**, Comparison of 3PM and 2PM images of fluorescein-labeled blood vessels in the deep cortex. Scale bar 30  $\mu\text{m}$ .

**b**, Intensity plot along the line profile along the blood vessel in Figure 8a at 900  $\mu\text{m}$ . Both 2PM and 3PM profiles were normalized to their respective maximum.

**c**, Comparison of 3PM and 2PM images of GCaMP6s-labeled neurons in deep cortex. Background fluorescence was measured within a big blood vessel (unstained), since the brain tissue was mostly filled with labeled dendrites (neuropil). Scale bar 30  $\mu\text{m}$ .

**d**, Normalized intensity plot along the line profile of the neuron in Figure 8c. The profile is decomposed into signal, neuropil and background fluorescence.

**e**, SBR curve measured on fluorescein-stained blood vessel and GCaMP6s-labeled neurons. Vertical error bars denote the standard deviation of SBR, and horizontal error bars represent the depth range of signal.

The major practical limitation on 2PM imaging depth is out-of-focus background generation instead of signal strength, when imaging in a densely labeled sample<sup>31</sup>. Figure 8a and b show the intensity profile across the same stained blood vessel, imaged by 2PM and 3PM simultaneously. At the depth of 780  $\mu\text{m}$ , 2PM shows strong background on the same order as the signal strength. To quantify the SBR for vascular images, the background is measured as the pixel values in the unstained areas surrounding the labeled blood vessels, and the signal as the pixel values of the labeled blood vessels (the top 0.1% brightest pixels) after subtraction of the background. For GCaM6s labeled neurons, the background is instead quantified as the pixel values in

the shadow of big blood vessels, since other regions of the tissue is stained by neuropil (Figure 8c and d). For both 2PM and 3PM, background is negligible on the sample surface with SBR  $\sim 100$  (Figure 8a, b and e). The actual SBR may be higher since the background was too low to be measured accurately. As the depth increases beyond 600  $\mu\text{m}$  in the cortex, 920-nm 2PM background started to increase rapidly, accompanied by obvious degradation of image quality (Figure 8a). The SBR for 2PM reaches  $\sim 1$  at about 780  $\mu\text{m}$  ( $\sim 5$  attenuation lengths in the mouse cortex), for both fluorescein labeled blood vessels and GCaMP6s labeled neurons (Figure 8e). In contrast, 1320-nm 3PM does not show change in background until much deeper in the white matter (Figure 8e).

### ***3.6 Estimate of Nonlinear Damage Threshold by 1320-nm Three-photon Microscopy***

Neurons can be sensitive to nonlinear damage by high peak power, which induces rapid ionization and recombination of molecules followed by pressure increase<sup>40</sup>. During this process, membranes of calcium concentrated organelles may be ruptured, leading to saturation of cytoplasmic calcium as well as calcium indicators, which can be observed as a sudden but irreversible elevation to extraordinary cell brightness. Our imaging experiments in the hippocampus show that neurons remain healthy and viable for weeks after hours of exposure to 1.5 nJ with 60 fs pulses at 1320-nm wavelength (Section 4)<sup>11</sup>. We observed that cell ablation can certainly happen with 10 nJ pulse energy (and 60 fs pulse duration) at the focus within minutes of continuous scanning. Therefore, we strongly advise keeping pulse energy

at the focus under 5 nJ for imaging.

### ***3.7 Estimation of Thermal Damage Threshold by 1320-nm Three-photon Microscopy by Monte Carlo Simulation***

As imaging depth increases, thermal damage eventually limits the maximum power as well as imaging depth achievable by 3PM, since the total power grows exponentially with depth.

Temperature rise caused by light absorption in brain disturbs normal neurophysiological functions. For example, even 1 °C increase above physiological temperature can result in higher neuron firing rates, and tissue damage happens at about 39 °C or above <sup>41</sup>. In order to obtain a quantitative understanding of tissue heating mechanisms by 1320-nm 3PM imaging, We employed Monte Carlo method to calculate 1320-nm light intensity distribution in the scattering tissue, based on which the spatial profile of temperature is numerically calculated with heat equation. Podgorski et al had previously applied the method to estimate tissue heating by 2PM, and verified the results with experimental measurement <sup>41</sup>. Here we shall state our findings briefly, and leave the details in APPENDIX A.

Despite the small tolerance margin for temperature rise in the tissue, heat dissipation and photon backscattering through the cranial window helps to significantly reduce tissue heating. With a cranial window exposed to immersion water at room temperature (~25°C), the brain surface temperature was measured to be

as low as 32.4°C in awake mice without any external heating source<sup>41</sup>. The temperature gradient across the window causes a constant heat loss of 15-45 mW from the brain, with more heat loss when the objective is closer to the window (Figure 23). Tissue scattering reduces heating in two ways: 1) Diffusive reflection by which backscattered photons exit sample surface without being absorbed. In fact, as much as 25% of total photons are eventually reflected back to the cranial window at 920 nm, and 9% for 1320 nm (Table 5). 2) The broadening of light intensity distribution allows some photons to escape the illuminated volume further away in the tissue, so that they do not contribute to the point of the maximum temperature. In fact, only 30% of input photons cause local heating at 920 nm, and 60% for 1320 nm (Table 5).

Under continuous 920-nm illumination, the thermal damage threshold is 250-300 mW in awake mouse with cranial window (NA=0.8; Linear FOV=1 mm; focal depth=250 µm)<sup>41</sup>. In comparison, 1320-nm light experiences stronger water absorption and weaker scattering, which implies higher heat generation in a smaller volume, and therefore a lower damage threshold is expected. According to the simulation, in order to keep the maximum temperature below 38 °C, the maximum power should not exceed 100 mW even beyond 1 mm imaging depth with continuous scanning at 1320 nm (Figure 22 and Figure 23). The simulation agrees with a previous experiment result where no damage was observed when 93 mW of 1280 nm applied on sample surface to image 1 mm deep<sup>7</sup>.

### 3.8 Optimization of System Parameters for Deep Imaging

In order to achieve the best performance for 1320-nm 3PM imaging of GCaMP6, the imaging system should be optimized following the procedures below:

1. Center the excitation spectrum at 1300-1320 nm with a FWHM  $> 50$  nm.

Compensate any dispersion in the entire optical system and ensure  $\leq 60$  fs pulse duration at the objective focus. Any clipping should be avoided in the beam path.

Since 3PE is sensitive to wavefront distortion. For deep imaging, the objective back-aperture should be under-filled to have  $1/e^2$  diameter of the Gaussian beam matching 70% of the objective back-aperture diameter<sup>2,42</sup>.

2. Verify the imaging system is shot-noise limited (detailed in Section 2.2).

Calculate the minimum signal photon counts required to detect a single spike in a shot-noise limited system  $N_d$  (Section 2.3). For example,  $N_d=100$  photons per second is needed for GCaMP6s when  $d^2=3$ .

3. Determine pulse energy at the focus for a desired signal yield  $Y$ . For example, given a 1320-nm pulse of duration  $\tau_0 = 60$  fs,  $E_0=1.8$  nJ is required to generate  $Y_0=0.1$

photon per excitation pulse from GCaMP6s at typical cellular concentration. Now the target signal yield  $Y$  can be scaled with pulse energy  $E$  and pulse width  $\tau$  according to

the relation:  $Y=Y_0 \left(\frac{E}{E_0}\right)^3 \left(\frac{\tau_0}{\tau}\right)^2$ . Meanwhile, the peak power  $(E/\tau)$  should be remained

at a safe level to avoid nonlinear damage.

4. After determining  $E$  and  $\tau$ , the minimum number of pulses per second hitting a ROI can be calculated:  $N_{ROI}=N_d/Y$ . In the example above, assuming  $Y=Y_0=0.1$ ,

$N_{ROI}=1000$  pulses per second is required.

5. Given the imaging depth  $z$ , pulse energy at the sample surface can be calculated according to exponential decay:  $E_{surf} = E \exp\left(\frac{z}{l_e}\right)$ . Continue with the example, when  $z=700 \mu\text{m}$ ,  $l_e = 300 \mu\text{m}$ ,  $E_{surf}= 18.6 \text{ nJ}$ . In order to convert to the pulse energy out of the objective, immersion water absorption should also be included. The pulse energy out of the objective can be calculated as  $E_{obj} = E_{surf} \exp(\mu_{app}Z_0)$ , where  $Z_0$  is the immersion water thickness, and  $\mu_{app}$  can be looked up in Figure 24 for different excitation wavelengths. Continue with the example, when  $Z_0=1140 \mu\text{m}$  and the excitation wavelength centers at  $1320 \text{ nm}$ ,  $E_{obj} = 23 \text{ nJ}$ .

6. If the laser repetition rate  $f$  is fixed, calculate the average power on the sample surface, and check if it would cause heating at the imaging depth (Figure 23).

Determine the imaging FOV, which in turn determines ROI dwell time, so that at least  $N_{ROI}$  photons land on the ROI for every second. For example, when acquiring with  $1.5 \text{ MHz}$  repetition rate,  $300 \mu\text{m} \times 300 \mu\text{m}$  FOV with  $90\%$  acquisition fill fraction, a typical neuron of  $\sim 100 \mu\text{m}^2$  area will receive  $50/(300 \times 300) \times 0.9 \times 3 \times 10^6 = 1500$  pulses per second, which is larger than  $N_{ROI} = 1000$  in the example above. Meanwhile, the average power at the sample surface is still below the thermal damage threshold:  $18.6 \times 3 \times 10^6 = 56 \text{ mW}$ .

7. If laser repetition rate is flexible, in order to have as big FOV as possible, the repetition rate should be increased until limited by the thermal damage (Figure 23).

To ensure successful 3PM imaging of GCaMP, care must be taken to optimize the system parameters and performance. Therefore, we have delineated the thresholds

for the nonlinear and thermal damage, and have casted new insights on how to reduce temperature rise in the tissue. For example, a bigger cranial window of  $> 4\text{mm}$  clearance diameter, will help deep tissue imaging in multiple ways: less chance of light clipping (since the light spot on brain surface has the radius close to imaging depth when  $\text{NA} \sim 1$ ), higher collection efficiency, and more heat dissipation and diffusive reflection of photons to reduce tissue heating. Meanwhile, unnecessary aberration can be avoided by simple measures, such as under-filling the objective back-aperture, optimizing the correction collar (if applicable), and leveling the cranial window parallel to the objective front window.

A larger FOV (e.g.  $1\text{ mm} \times 1\text{ mm}$ ) of 3PM calcium imaging in the deep cortex may be possible with a higher laser repetition rate up to 4 MHz (which will approach thermal damage limit), lower spike detection sensitivity (for example, detecting 2 action potential induced spikes takes only 1/4 of the signal strength as 1 action potential induced spikes), and the brighter calcium indicators that are soon available.

## CHAPTER 4

### 4 THREE-PHOTON CALCIUM IMAGING IN THE MOUSE HIPPOCAMPUS

As an important application of 3PM calcium imaging, we demonstrated spontaneous activities of up to 150 neurons in the hippocampal *stratum pyramidale* (SP) at ~1-mm depth within an intact mouse brain. As discussed in Section 3.5, similar imaging depth with green dyes exceeds the SBR limit of 2PM, and 2PM imaging of the mouse hippocampus had only been demonstrated with cortex removed<sup>12,13</sup>. Therefore, our method creates new opportunities for minimally invasive recording of neuronal activity with high spatial and temporal resolution beyond the depth limit of 2PM.

#### 4.1 *In vivo* Three-photon Calcium Imaging of GCaMP6s Neurons in the Hippocampus in Intact Mouse Brains

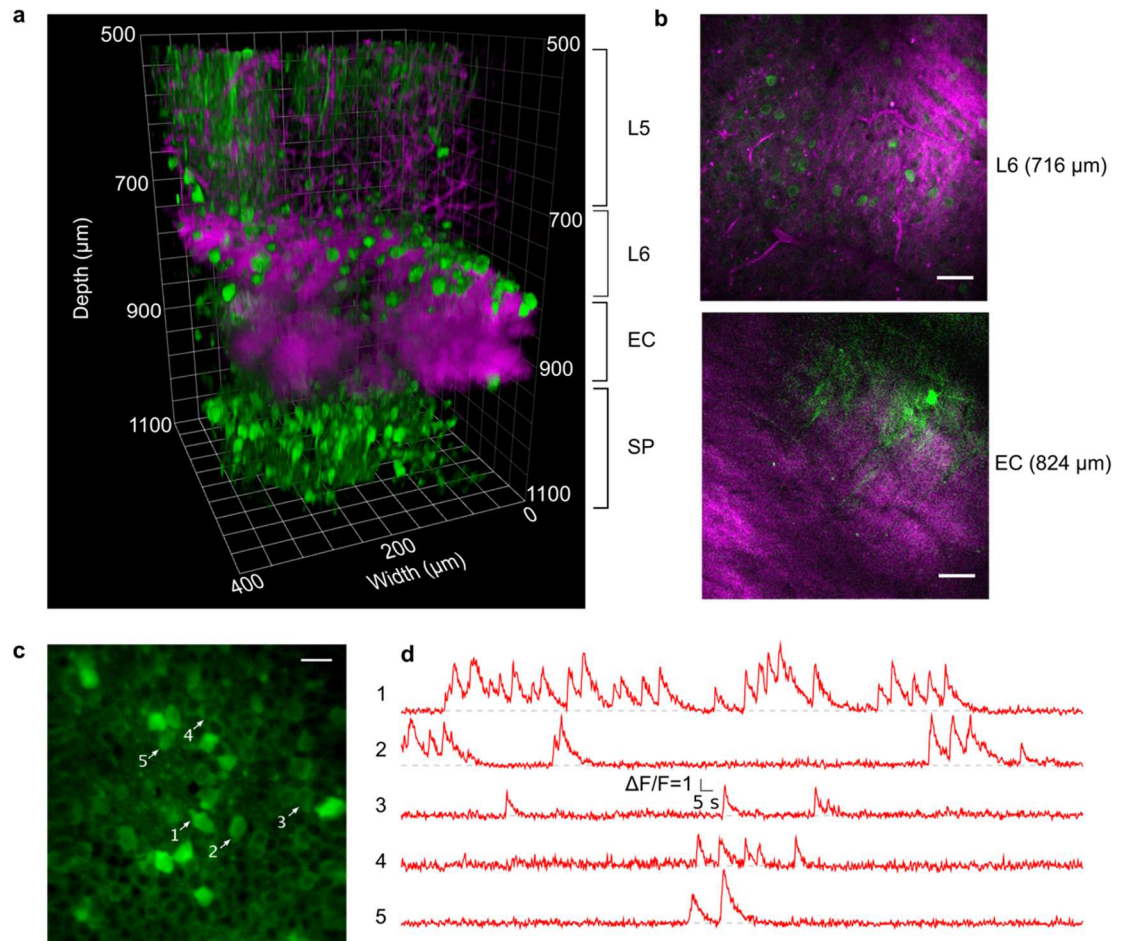


Figure 9. 3PM Imaging of Neuronal Structure and Function in the SP Layer of the Mouse Hippocampus

**a**, 3D reconstruction of 3PM images of GCaMP6s-labeled neurons in the mouse cortex and the hippocampus (green, fluorescence; magenta, THG.). See Supplementary Video 1 for individual XY frames of the z-stack.

**b**, Selected XY frames at various depths in **a**. THG visualizes blood vessels and myelinated axons (green, fluorescence; magenta, THG). Scale bars, 50  $\mu\text{m}$ .

**c**, Activity recording site in the SP layer of the hippocampus located at 984

$\mu\text{m}$  beneath the dura with a field-of-view of  $200 \times 200 \mu\text{m}$ . Scale bar,  $20 \mu\text{m}$ .

**d**, Spontaneous activity recorded from the labeled neurons indicated in **c**. Additional traces from 30 active neurons are shown in Figure 11 and Figure 12. The structural and functional imaging in this figure is representative of data from five animals.

We performed 3PM imaging of both the structure and activity of neurons in the SP layer of the mouse hippocampus (Figure 9). The hippocampal neurons were transfected by AAV virus expressing GCaMP6s (synapsin promoter, AAV2/1 encapsulation) in wild-type mice (C57BL/6J) (detailed in APPENDIX C). The imaging took place in the third to fifth week after injection (11–16-weeks-old mice). For structural imaging, we acquired a stack from 500 to 1100  $\mu\text{m}$  (3D reconstruction in Figure 9a). Labeled neurons in cortical layer 6 are visible immediately above the external capsule (EC), where myelinated axons display strong third harmonic generation (THG) signals (Figure 9a and b). THG is a third order nonlinear process that happens at various interfaces of refractive index and nonlinear susceptibility ( $\chi^{(3)}$ ) contrast<sup>43</sup> (e.g., blood vessels and myelinated axons). Another benefit of 3PM is that it is always accompanied by THG at visible wavelength, which provides additional structural information without any exogenous labeling. The EC features fibrous structure (Figure 9b) extending approximately from 730 to 860  $\mu\text{m}$  below the dura (Figure 9a). GCaMP6s-labeled neurons in the SP layer span from 940 to 1040  $\mu\text{m}$  below the surface and begin  $\sim 80 \mu\text{m}$  below the EC. Labeled neurons display clear nuclear exclusion and the characteristic honeycomb arrangement of the SP layer

(Figure 9c). The distinctly resolved neuron morphology at ~1 mm below the dura shows that 3PM is capable of high-spatial-resolution imaging deep within an intact mouse brain.

We imaged spontaneous activity from the hippocampal neurons at the site shown in Figure 9c. We were able to image a population of up to 150 neurons, acquiring fluorescence time traces of neurons of different brightness (Figure 9d). A high signal-to-noise ratio was achieved, which was indicated by the absolute photon counts per neuron per frame (Figure 10b). We recorded continuously at a frame rate of 8.49 Hz ( $256 \times 256$  pixels/frame) for up to 48 minutes in one imaging session with a FOV of  $200 \times 200 \mu\text{m}$  (Figure 10, Figure 11, and Figure 12). The average power used was ~50 mW, and no noticeable photo-bleaching or photo-toxicity was observed throughout the entire recording session (Figure 11 and Figure 12).

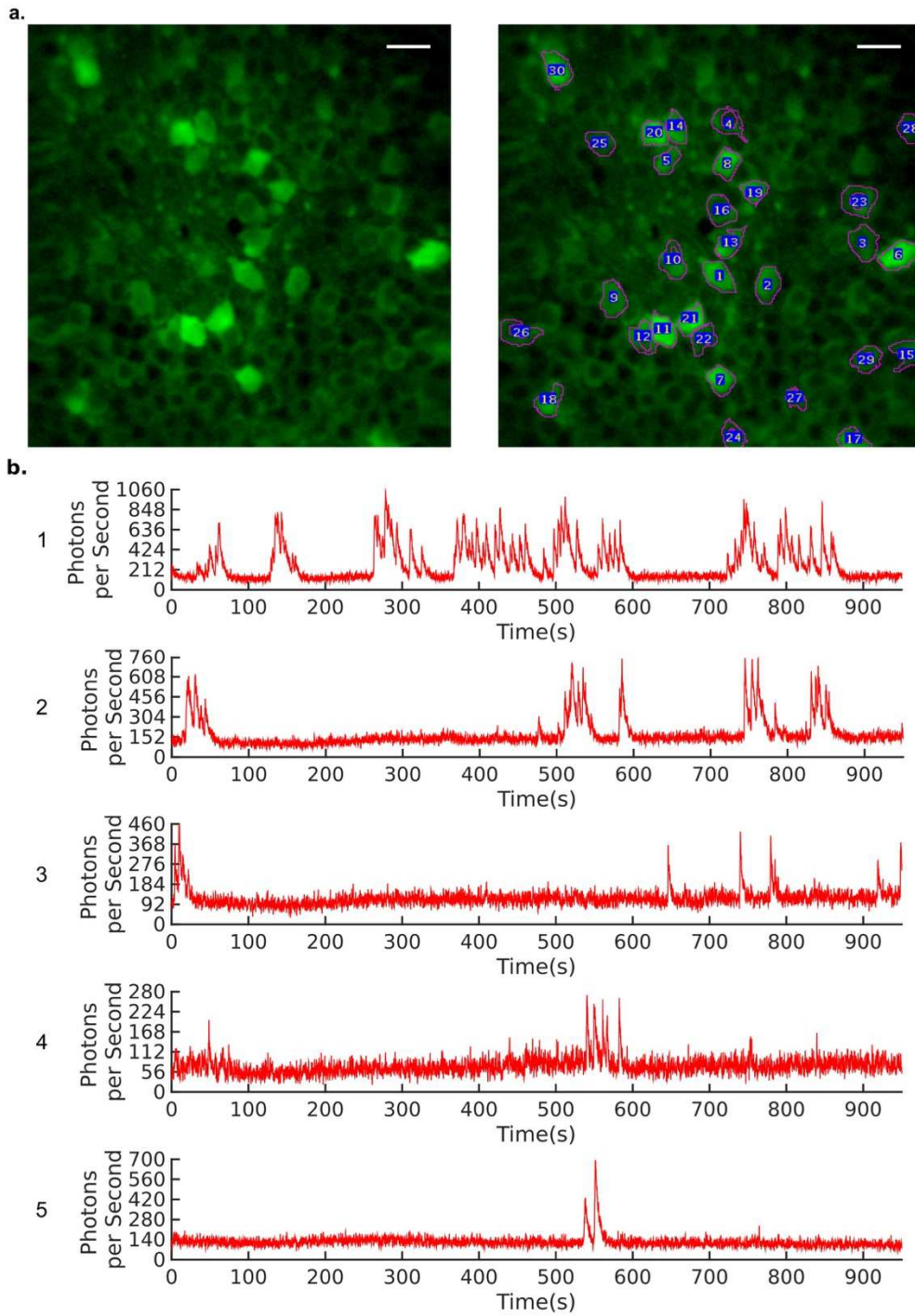


Figure 10. 3PM Imaging of Spontaneous Activity in GCaMP6s-labeled Neurons in the SP Layer of the Mouse Hippocampus

**a,** 3PM image of neuronal population in the CA1 region of the hippocampus

located at 984  $\mu\text{m}$  beneath the dura (left). Neurons are indexed (right) for reference to traces in (b), Figure 11 and Figure 12. Average power of 50 mW at 800 kHz repetition rate was used for imaging. The FOV was 200x200  $\mu\text{m}$ . Scale bar, 20  $\mu\text{m}$ .

**b**, Spontaneous activity traces plotted in the unit of photon counts, recorded from neuron 1-5 in (a) during approximately the first 16 minutes of a 48-minute recording session, at a frame rate of 8.49 Hz. The five neurons represent a range of activity level and brightness. All traces were low-pass filtered with a hamming window with a 0.59 s time constant, and fluorescence intensity was converted to photon counts per neuron per second.

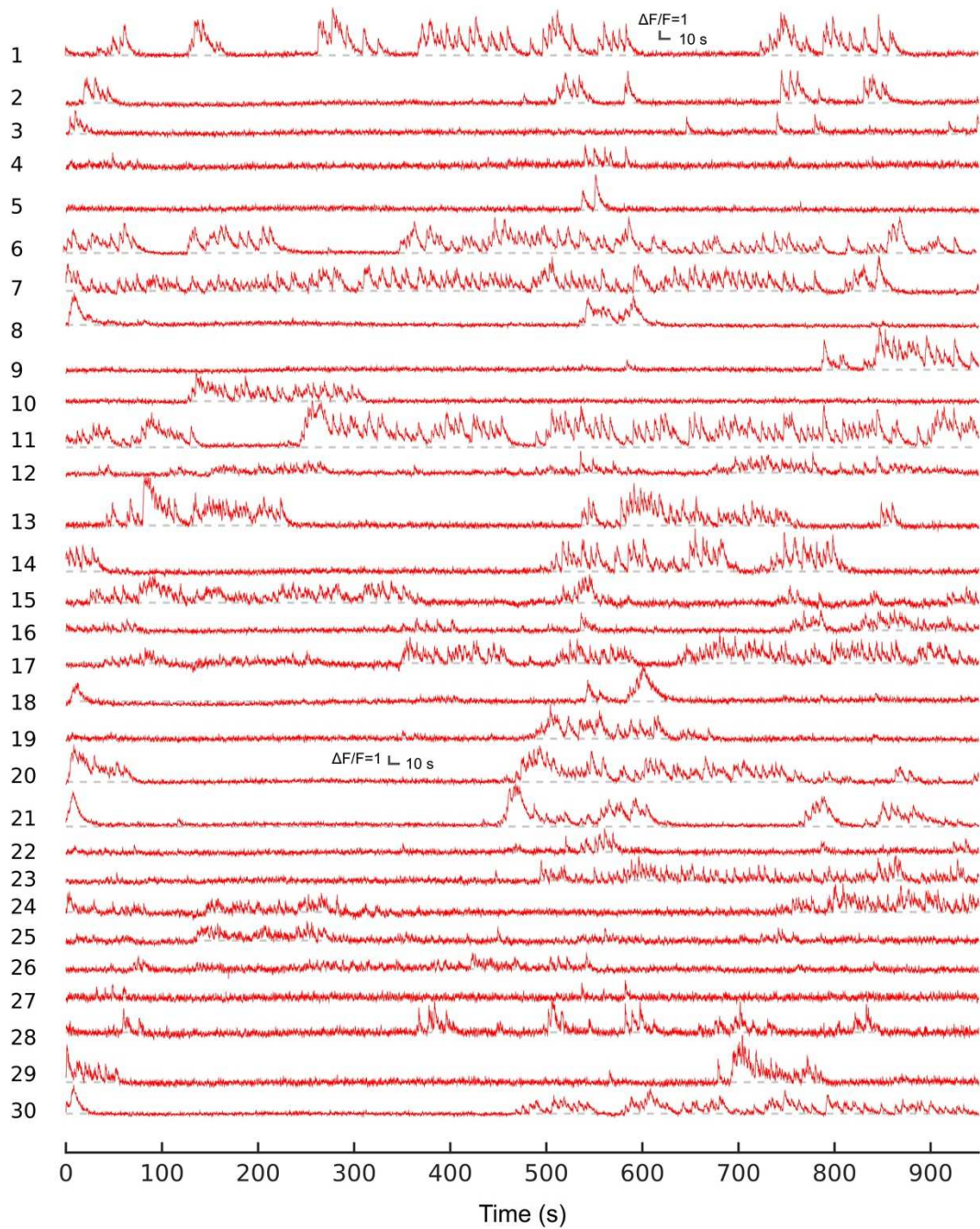


Figure 11. Spontaneous Activity Traces of the Hippocampal Neurons Shown in Figure 10

Spontaneous activity traces recorded from all the indexed neurons in Figure 10 during approximately the first 16 minutes of a 48-minute recording

session, at a frame rate of 8.49 Hz. To the left of each trace is the index of the neuron. All traces were low-pass filtered with a hamming window with a 0.59 s time constant, and then normalized to each individual baseline.

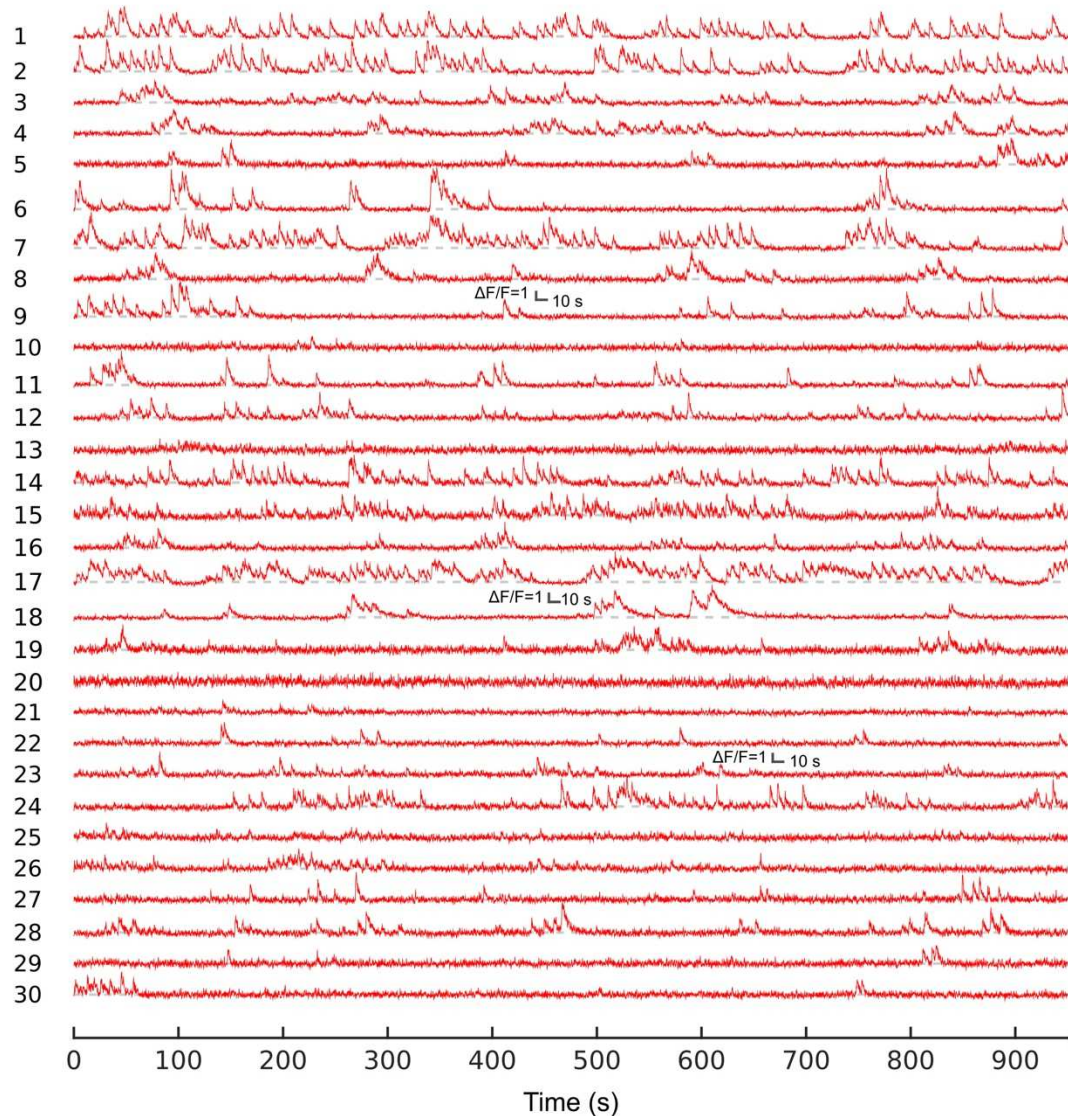


Figure 12. Continued Recording of Spontaneous Activities from the Same Hippocampal Neurons in Figure 10

Spontaneous activity traces recorded from the same neurons in Figure 10 during approximately 16 minutes after 32 minutes of continuous recording (i.e., approximately the last 16 minutes of the 48-minute recording session

starting in Figure 11).

#### ***4.2 Damage Consideration of Three-photon Calcium Imaging***

Imaging the mouse brain at 1280 nm with average power up to 120 mW did not result in any noticeable tissue damage<sup>7</sup>. However, the higher intensities required by the nonlinear excitation might induce sample change or damage. We performed deep cortex and hippocampus imaging by scaling the pulse energy with imaging depth to ensure less than 1.5 nJ at the focal plane. By continuous imaging the same neuronal population for as long as 48 minutes, we confirmed no noticeable photo-bleaching or photo-toxicity was induced in the cells (Figure 11 and Figure 12). Furthermore, we revisited the same site multiple times spanning many days after the first imaging session, and we successfully recorded neuronal activity from the same population of neurons each time (Figure 13 and Figure 14).

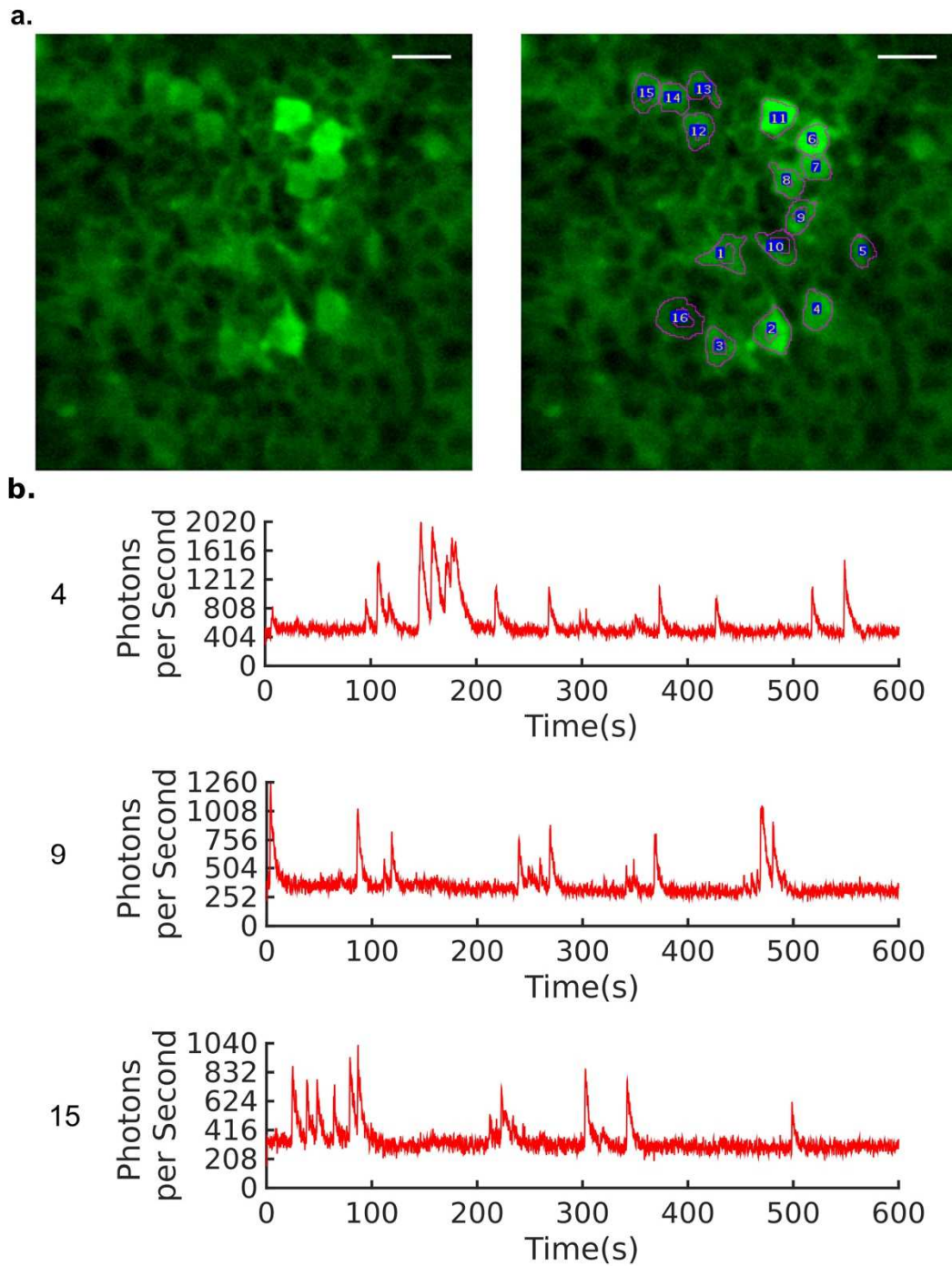


Figure 13. Revisit of the Same Neuronal Population in the SP Layer of the Hippocampus after One Week

**a,** Activity recording site in the SP layer of the hippocampus located at 984

$\mu\text{m}$  beneath the dura (left). The neuronal population was the same as that shown in Figure 9 and Figure 10, but imaged one week later. Neurons are indexed (right) for reference to their traces in (b) and Figure 14. Average power of 58 mW at 800 kHz was used for imaging. The FOV was 150x150  $\mu\text{m}$ . Scale bar 20  $\mu\text{m}$ .

**b**, Spontaneous activity traces recorded from three indexed neurons in (a) for 10 minutes, at a frame rate of 8.49 Hz. The three neurons represent a range of activity level and brightness. To the left of each trace is the index of the neuron. All traces were low-pass filtered with a hamming window with a 0.59 s time constant, and fluorescent intensity was converted to photon counts per neuron per second.

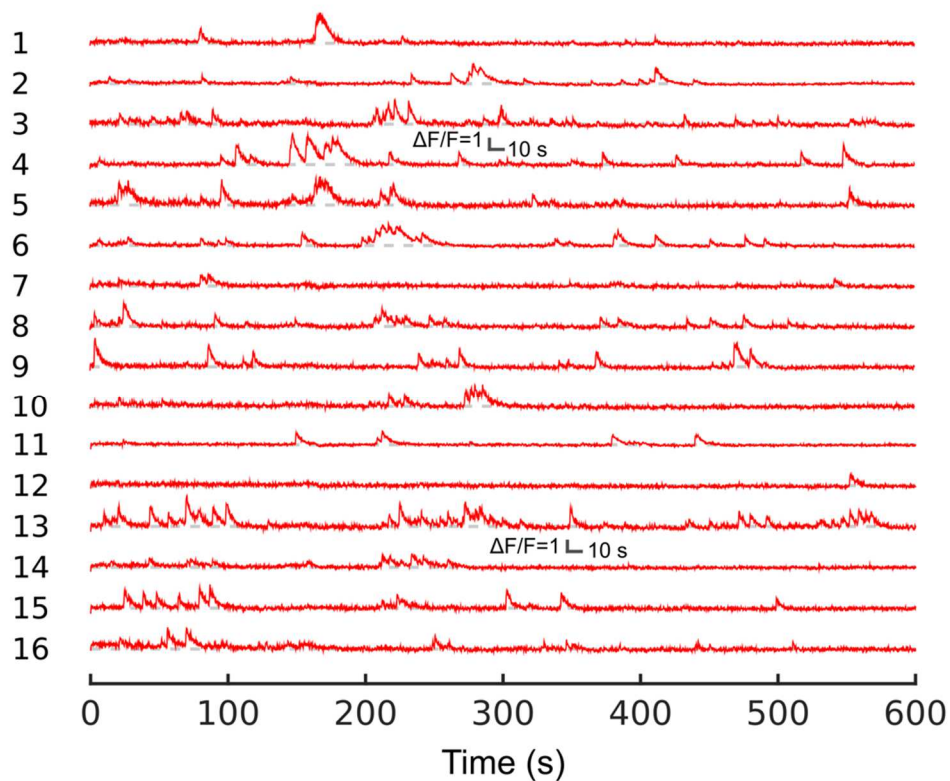


Figure 14. Spontaneous Activity Traces of the Hippocampal Neurons Shown in Figure 13

Spontaneous activity traces recorded from all indexed neurons in Figure 13 for 10 minutes, at a frame rate of 8.49 Hz. All traces were low-pass filtered with a hamming window with a 0.59 s time constant, and then normalized to each individual baseline.

### **4.3 Conclusions**

3PM can record activity from a large number of neurons with high spatial and temporal resolution deep within scattering brain tissues. An additional feature of 3PM is the intrinsic THG signal generated at various interfaces (e.g., blood vessels and myelinated axons; Figure 9), which provides additional structural information without an exogenous stain. Imaging the spontaneous activity in the hippocampal SP layer within an intact mouse brain is just one such demonstration, and the application of our method will enable studies that require noninvasive, high-resolution imaging deep within scattering tissue.

## CHAPTER 5

### 5 THREE-PHOTON CALCIUM IMAGING THROUGH THE INTACT MOUSE SKULL

As demonstrated in the previous sections, the long wavelength 3PM has advantages in deep imaging in densely labeled samples (but with mild aberration). In addition, we find the higher nonlinear confinement of 3PE also significantly improves penetration through highly scattering and turbid layers, such as the intact mouse skull, which induces strong scattering and aberration on the transmitted optical field. We find that 3PE improves optical sectioning compared to 2PE, even with the same excitation wavelength and imaging system. Through the adult mouse skull, we demonstrate three-photon imaging of vasculature at  $>500\mu\text{m}$  depth, and GCaMP6-calcium imaging over weeks in cortical layers 2/3 and 4 in awake mice, with 8.5 frames/s and hundreds of micrometers FOV.

#### ***5.1 The Scientific Significance and the Status Quo of Through-skull Imaging***

Observing the mouse brain in its native environment is critical to the study of neural network function and disease progression<sup>44</sup>. Cranial window implantation<sup>45</sup> and skull thinning<sup>46,47</sup> are the common minimally invasive procedures to obtain optical access to the mouse brain; however, they can still cause perturbation to the physiological environment in some cases. For example, mechanical stress during the surgeries induce unexpected activation of microglia and astrocytes<sup>46,48</sup>; skull openings change

intracranial pressure and affects fluid flow in paravascular space, which may be important for waste disposal<sup>49</sup>. Therefore, improving imaging performance through the intact skull will open new opportunities to non-invasive brain research.

Non-fluorescence based technologies such as magnetic resonance imaging<sup>50</sup>, photoacoustic tomography<sup>51</sup>, and optical microangiography<sup>52</sup> can map brain structure and hemodynamics below an intact skull. However, these technologies typically cannot achieve single-cell or sub-cellular resolution, and none of them is established for direct cellular activity measurement with high temporal resolution (e.g., > 1 Hz).

One-photon fluorescence can be used for imaging vasculature and neuronal activity through skull, either with infrared dyes<sup>53</sup>, or skull clearing techniques<sup>54,55</sup>. However, such methods generally do not offer single-cell resolution, due to out-of-focus fluorescence excitation.

Two-photon microscopy (2PM) is routinely used for *in vivo* deep brain imaging for its optical sectioning capability in scattering media<sup>31</sup>; however, 2PM has poor resolution when imaging through an intact skull<sup>56</sup>. Although wavefront correction enabled 2PM to achieve submicron resolution, the corrected field-of-view (FOV) was about 23x23  $\mu\text{m}$  and the imaging depth was limited to approximately 50  $\mu\text{m}$  in the cortex<sup>56</sup>. Recently, chemical treatment of the skull surface has been applied to improve the contrast of structural 2PM in the shallow cortex<sup>57,58</sup>.

Three-photon microscopy (3PM) increases the imaging depth in the mouse brain because of the weaker scattering at longer excitation wavelengths and the background suppression by higher order nonlinear excitation, and 3PM imaging studies

have revealed structure and function in the mouse hippocampus through cranial windows in intact brains<sup>10,11</sup>. Recently, vasculature imaging through the intact mouse skull was demonstrated with a synthesized dye of unusually large three-photon excitation (3PE) cross section at 1550 nm, reaching a depth of 300  $\mu\text{m}$ <sup>59</sup>. In this study, we show that 3PM not only achieves more than 500  $\mu\text{m}$  cortical depth with conventional dyes but also is capable of calcium activity imaging at high spatial and temporal resolution with hundreds of micrometers FOV.

## ***5.2 Three-photon Excitation Enhances Optical Sectioning through the Intact Mouse Skull***

The refractive index of the cranial bone ( $\sim 1.55$ ) is significantly higher<sup>60</sup> than that of water (1.32) or cerebrospinal fluid ( $\sim 1.34$ )<sup>33</sup>. The high refractive index and the rough skull surface, especially after exposed to air<sup>54</sup>, renders the skull opaque by scattering light like optical diffusers. We found that the skull surface roughness can be reduced by using an index-matching glue, which also seals the skull from the air and preserves transparency for chronic imaging (Figure 15a). After the treatment, the effective attenuation length<sup>10</sup> ( $l_e$ ) of the skull was measured using the third harmonic generation (THG) signal from the osteocytes, and we found  $l_e \sim 60 \mu\text{m}$  at 1320 nm (Figure 15d).

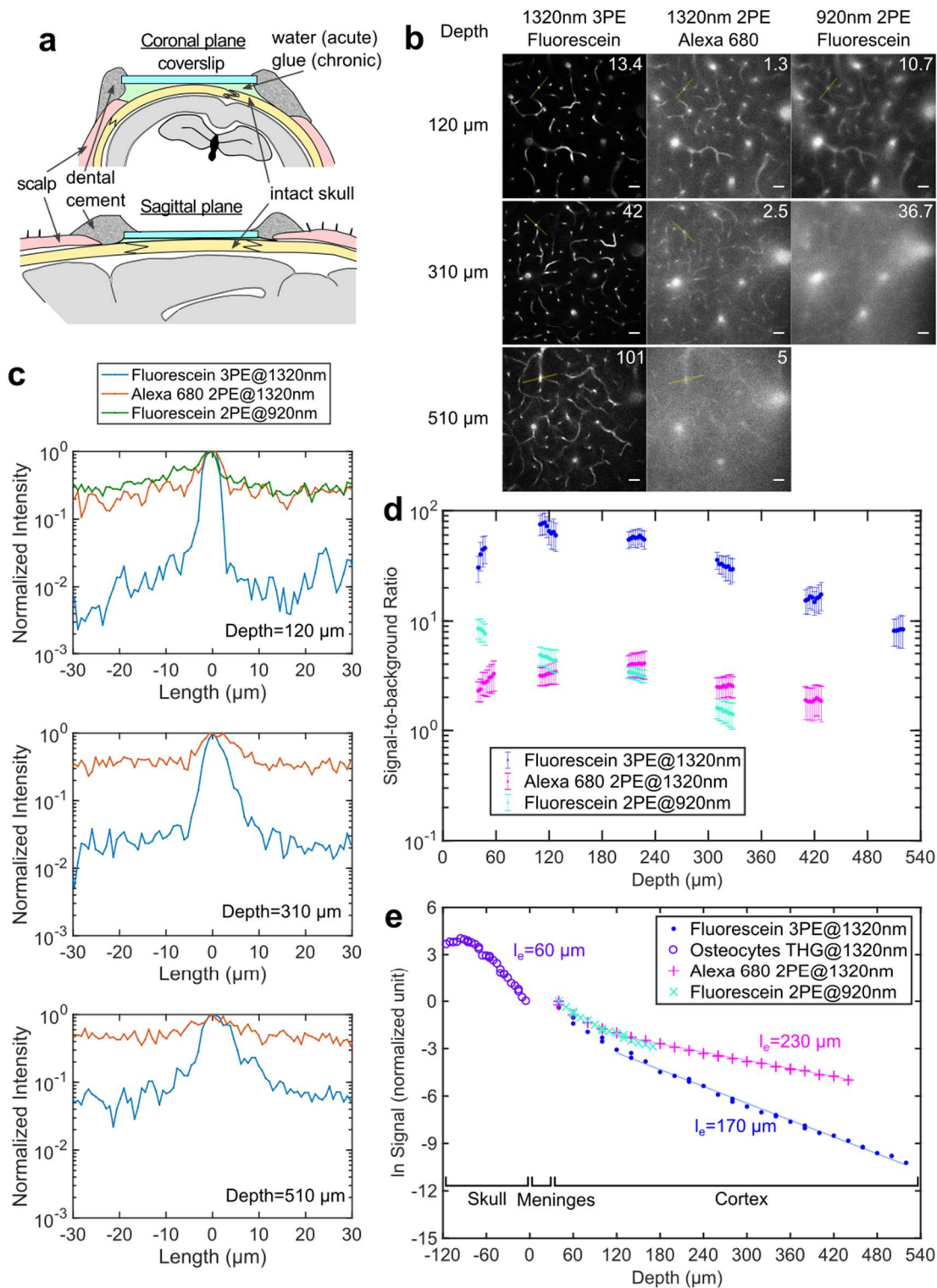


Figure 15. Comparison of Through-skull Vasculature Imaging by 3PM and 2PM.

**a**, Schematic of through-skull imaging preparation with sagittal and coronal views (photos of a good preparation are shown in Figure 25).

**b**, Comparison of 2PM and 3PM images of vasculature of a wild-type mouse (C57BL/6J, male, 12 weeks, similar results  $n=3$ ) in the same cortical column under the central area of a parietal bone, with chronic preparation. Each site was imaged by 920-nm 2PE of fluorescein, 1320-nm 3PE of fluorescein and 1320-nm 2PE of Alexa680 during the same imaging session. For 920-nm 2PM, 510  $\mu\text{m}$  depth is not shown since the maximum imaging depth achieved was 420  $\mu\text{m}$ . The number in the upper right corner of each frame indicates the average power used in unit of mW. Each frame was integrated for 50 s to ensure photon shot noise is negligible, and all image contrasts were linearly stretched to saturate top 0.2% pixels. Scale bar, 30  $\mu\text{m}$ .

**c**, Intensity profiles across the brightest blood vessels in each frame in **(b)**, along the yellow lines (similar results  $n=3$ ).

**d**, SBR measured at different depths for the three imaging groups in **(b)** (similar results  $n=2$ ). The signal was calculated from the average of the top 0.1% brightest pixels in each frame, and background from the average of the unlabeled regions. Each data point was calculated from one image, and the vertical error bar indicates the standard deviation of SBR, originated from the brightness variation of blood vessels in each image.

**e**, Signal attenuation with depth for through-skull vasculature imaging measured in the same mouse as in **(b)** (similar results,  $n=2$ ). Meninges include dura mater, arachnoid and pia mater. The signal strength at a particular depth is represented by the average value of the brightest 0.5% of the pixels in the x-y image from that depth. The effective attenuation length  $l_e$  was determined by the exponential fit of the signal as a function of imaging depth (THG signal was used inside the skull). Each data point was calculated from one image.

We compared 2PM at 920 nm and 3PM at 1320 nm by imaging fluorescein-labeled vasculature of the same mouse, through the intact skull around the center of the parietal bone. 1320-nm 3PM resolved capillary vessels with high contrast (Figure 15b), with signal-to-background ratio (SBR) close to 100 at 120  $\mu\text{m}$  cortical depth, and  $\sim 10$  at 510  $\mu\text{m}$  (Figure 15c). In comparison, 920-nm 2PM has substantially lower contrast, with tens of times higher background in the unlabeled region of the brain even at shallow depths (Figure 15c). We verified that 920 nm generates negligible intrinsic autofluorescence in the emission band of fluorescein by imaging the mouse before any dye injection. Therefore, the background in 2PM is fluorescence from fluorescein.

To delineate the effects of longer wavelength and the higher order nonlinear excitation in through-skull imaging, we injected Alexa 680 into the same mouse, and immediately performed imaging by two-photon excitation (2PE) of Alexa 680 with 1320 nm, using the same laser and microscope. Figure 15c and d indicate that the 1320-nm 2PM has similar SBR as 920-nm 2PM at all depths, with only limited improvement on contrast, presumably by the reduced scattering and aberration at the longer excitation wavelength (Figure 15b, the background was also verified to be fluorescence from Alexa 680). These results show that longer excitation wavelength alone is not sufficient, and 3PE is necessary for through-skull imaging.

With cranial windows, the SBR of 2PM remains high until the imaging depth is beyond approximately 4 scattering lengths<sup>31</sup>. However, in our through-skull experiment, the SBR of 2PM, even with 1320 nm excitation, is below 10 immediately beneath the

skull (Figure 15c and d). The skull accounts for approximately 2 attenuation lengths, and has low labeling density due to the sparsity of vasculature in the bone. Therefore, the background in 2PM must be caused by the degradation of the point spread function (PSF), in both lateral (XY) and axial (Z) dimensions. For example, the lateral broadening of PSF is indicated by the blurred edges of capillaries in 2PM images (Figure 15b); the axial elongation is indicated by the observation that large, penetrating blood vessels are much brighter relative to horizontal capillaries in 2PM than in 3PM (Figure 15b). The higher order nonlinear excitation of 3PM is more effective in accentuating the central peak (i.e., the signal) and suppressing the unwanted fluorescence excitation from the side lobes (i.e., the background) of the PSF. Therefore, 3PE helps to preserve spatial resolution and improve image contrast with a degraded PSF.

The degradation of PSF is further corroborated by the reduced attenuation length of the brain tissue for through-skull imaging. The measured effective attenuation length ( $l_e=170 \mu\text{m}$ , Figure 15e) in the neocortex for through-skull 3PM is much shorter than that measured with cranial windows ( $\sim 300 \mu\text{m}$  throughout the entire neocortex<sup>61</sup>). Such rapid signal attenuation can only be explained by the deterioration of the PSF in through-skull imaging. Since the decay of fluorescence collection efficiency is small in relatively shallow imaging depths ( $< 500 \mu\text{m}$ ), and the different pulse durations used in 2PM and 3PM has no measurable impact on attenuation length (Figure 16). As the imaging depth increases, the beam size at the skull surface also increases, which can lead to significant aberration due to the heterogeneity of the skull. As the PSF deteriorates with increasing imaging depth, less signal is generated from the focal volume and more background is produced in the wings of the PSF, even with 3PE. This is corroborated by the decline in

the SBR for through-skull 3PM (Figure 15d), which has an SBR  $\sim 10$  at the imaging depth of  $\sim 500 \mu\text{m}$ . Previous work of 3PM with cranial windows achieved SBR  $\sim 100$  at  $> 1000 \mu\text{m}$  imaging depth<sup>10</sup>. The measured effective attenuation length for through-skull imaging reflects the combined effect of scattering by the brain tissue and wavefront distortion by the skull. Therefore, the effective attenuation length of the brain tissue in through-skull 3PM is much shorter than that with imaging through the cranial window.

The deterioration of the PSF also explains why the measured EAL for 2PM is significantly different from 3PM, even with the same excitation wavelength and the same mouse brain (Figure 15e). For example, the measured EAL ( $l_e$ ) for through-skull 2PM ( $l_e=230 \mu\text{m}$ ) is longer than that of 3PM ( $l_e=170 \mu\text{m}$ ) (Figure 15e). In fact, for through-skull 2PM, the axial elongation of the PSF causes significant background contribution to the detected fluorescence even at shallow depth (Figure 15b). Because the background fluorescence does not decrease rapidly with imaging depth, this leads to the apparent reduction in attenuation of the detected fluorescence for through-skull 2PM (Think of an extreme case where a Bessel beam is used, the attenuation cannot be measured due to the lack of axial resolution.). In comparison, 3PE enhances the axial resolution and thus more realistically reflects the actual attenuation of the excitation wavelength.

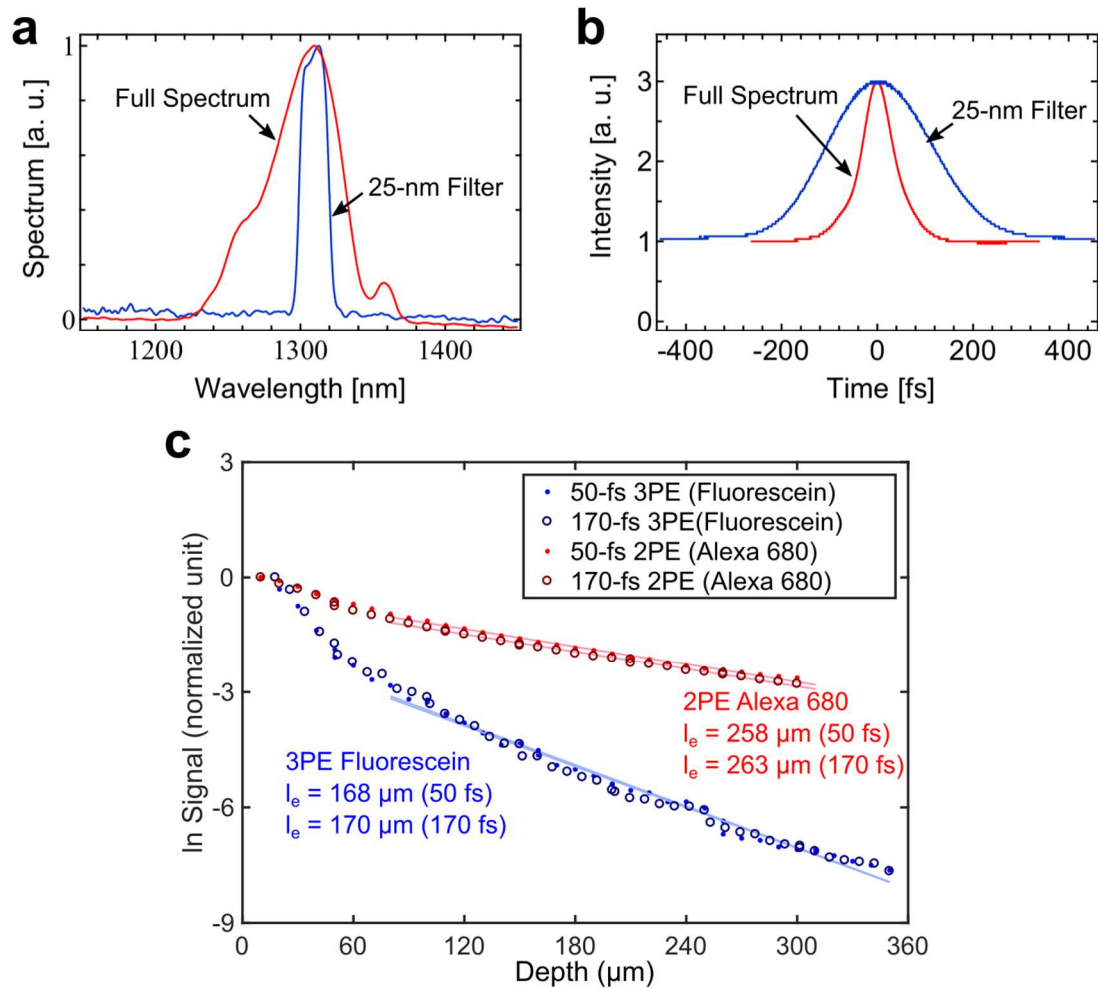


Figure 16. Tissue Attenuation Length vs Excitation Pulse Duration.

**a**, The full spectrum of the excitation pulses and the spectrum filtered by a 25-nm bandpass filter (a.u. means arbitrary units;  $n=3$ ).

**b**, Intensity autocorrelation traces of the original pulses and the spectrally filtered pulses. The measurements were performed under the objective, and the pulse durations were measured to be 50 fs and 170 fs, respectively, assuming  $\text{sech}^2$  pulse shape (a.u. means arbitrary units;  $n=3$ ).

**c**, The effective attenuation lengths measured through an intact skull of  $\sim 120 \mu\text{m}$  thickness ( $n=2$ ). The experiment setup was similar to that used for Fig. 1e, except that pulses of 50 fs and 170 fs were used to measure the attenuation lengths. The effective attenuation lengths were measured for

3PE of fluorescein and 2PE of Alexa 680. Despite the large difference in pulse duration, the difference in the effective attenuation lengths is negligible.

### 5.3 Through-Skull Neuronal Structural and Functional Imaging by Three-photon Microscopy

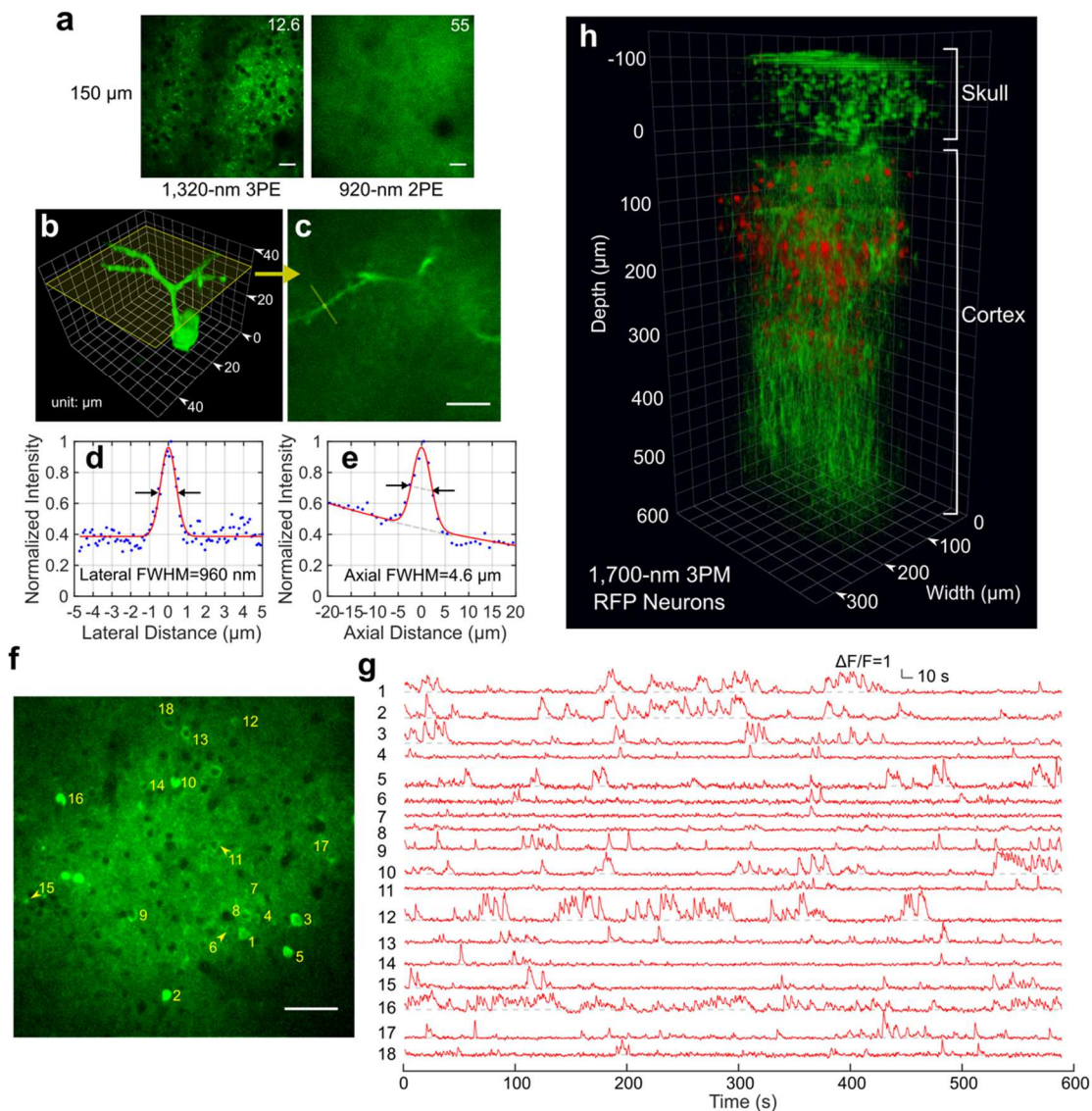


Figure 17. Through-skull Imaging of Neural Structure and Function

**a**, Comparison of 920-nm 2PM and 1320-nm 3PM through-skull imaging of neurons in a transgenic mouse (*CamKII-tTA/tetO-GCaMP6s*, female, 10 weeks) at 150  $\mu\text{m}$  cortical depth with  $\sim 105 \mu\text{m}$  skull thickness. The number in the upper right corner of each frame indicates the average power used in unit of mW. Each frame was integrated for 40 s. Scale bar, 20  $\mu\text{m}$ .

**b**, Comparison of 920-nm 2PM and 1320-nm 3PM through-skull imaging of neurons in a transgenic mouse (*CamKII-tTA/tetO-GCaMP6s*, female, 10 weeks) at 150  $\mu\text{m}$  cortical depth with  $\sim 105 \mu\text{m}$  skull thickness. Each frame was integrated for 40 s. Scale bar, 20  $\mu\text{m}$ . 3D reconstruction of a GCaMP6s-labeled neuron located about 140  $\mu\text{m}$  below the cortical surface of a transgenic mouse (*CamKII-tTA/tetO-GCaMP6s*, 10 weeks; similar measurements were performed on 2 mice with 3 neurons each, in total  $n=6$ ) imaged by 1320-nm 3PM through the intact skull (thickness  $\sim 100 \mu\text{m}$ ). Apical dendrites can be clearly observed for resolution estimation.

**c**, A cross section of the 3D stack in **(a)**, with its location indicated by the yellow frame in **(b)**. The locations for lateral and axial resolution measurement on the apical dendrite are indicated by the yellow line and circle, respectively (similar results  $n=6$ ). Scale bar, 10  $\mu\text{m}$ .

**d**, Lateral intensity profile measured along the yellow line in **(c)**, fitted by a Gaussian profile for the estimation of the lateral resolution (similar results  $n=6$ ).

**e**, Axial intensity profile measured in the region within the yellow circle in **(c)**, fitted by the sum of two Gaussian profiles, with one broad, off-centered Gaussian profile to correct for the uneven baseline, and the other for the central peak (similar results  $n=6$ ).

**f**, High resolution image of a site for through-skull activity recording in an awake, GCaMP6s-labeled transgenic mouse (*CamKII-tTA/tetO-GCaMP6s*, female, 8 weeks, similar results  $n=5$ ). The recording site is about 275  $\mu\text{m}$  below the cortical surface and the FOV was 320  $\mu\text{m}$  x 320  $\mu\text{m}$  (256x256 pixels per frame). Scale bar, 50  $\mu\text{m}$

**g**, Spontaneous activity traces recorded under awake condition from the indexed neurons in **(f)**, acquired at 8.49 Hz frame rate (similar results  $n=5$ ). The repetition rate used for imaging was 800 kHz, and the average power under the objective lens was 44 mW. Each trace is normalized to its baseline

and low-pass filtered by a hamming window of 1.06 s time constant. The same site was visited 8 times over a period of 4 weeks after the skull preparation, with cumulatively over 6 hours of recording time (data from other imaging sessions are shown in Figure 18).

**h**, 3D reconstruction of through-skull imaging of a cortical column of red fluorescent protein (RFP) labeled neurons in a Brainbow mouse (*B6.Cg-Tg(Thy1-Brainbow1.0)HLich/J*, male, 12 weeks, similar results n=2). The red channel is 3PE fluorescent signal from RFP and the green channel is THG. The zero depth is set just beneath the skull.

We imaged spontaneous activities of GCaMP6s-labeled neurons in adult transgenic mice (*CamKII-tTA/tetO-GCaMP6s*, 8-12 weeks, including both male and female, N=5). To provide an upper bound estimate of the spatial resolution of through-skull imaging, we measured the fluorescence intensity profile of a dendrite (Figure 18b-e). The lateral and axial FWHM is 0.96  $\mu\text{m}$  and 4.6  $\mu\text{m}$ , respectively, which provides the upper bound of the spatial resolution due to the finite size of the neural processes. 2PM at 920 nm could not resolve any feature at high spatial resolution using the same GCaMP6 mice (Figure 17a). Figure 17f shows an imaging site in cortical layer 2/3 of an 8-week-old mouse with  $\sim 120\text{-}\mu\text{m}$ -thick skull. The neuronal activity traces were recorded under awake condition (Figure 17g).

In addition to 1320-nm 3PM, we tested 1700-nm 3PM for through-skull structural imaging using red-fluorescent-protein labeled, reaching more than 500  $\mu\text{m}$  cortical depth (Figure 17h).

## 5.4 Longitudinal Three-photon Through-skull Calcium Imaging

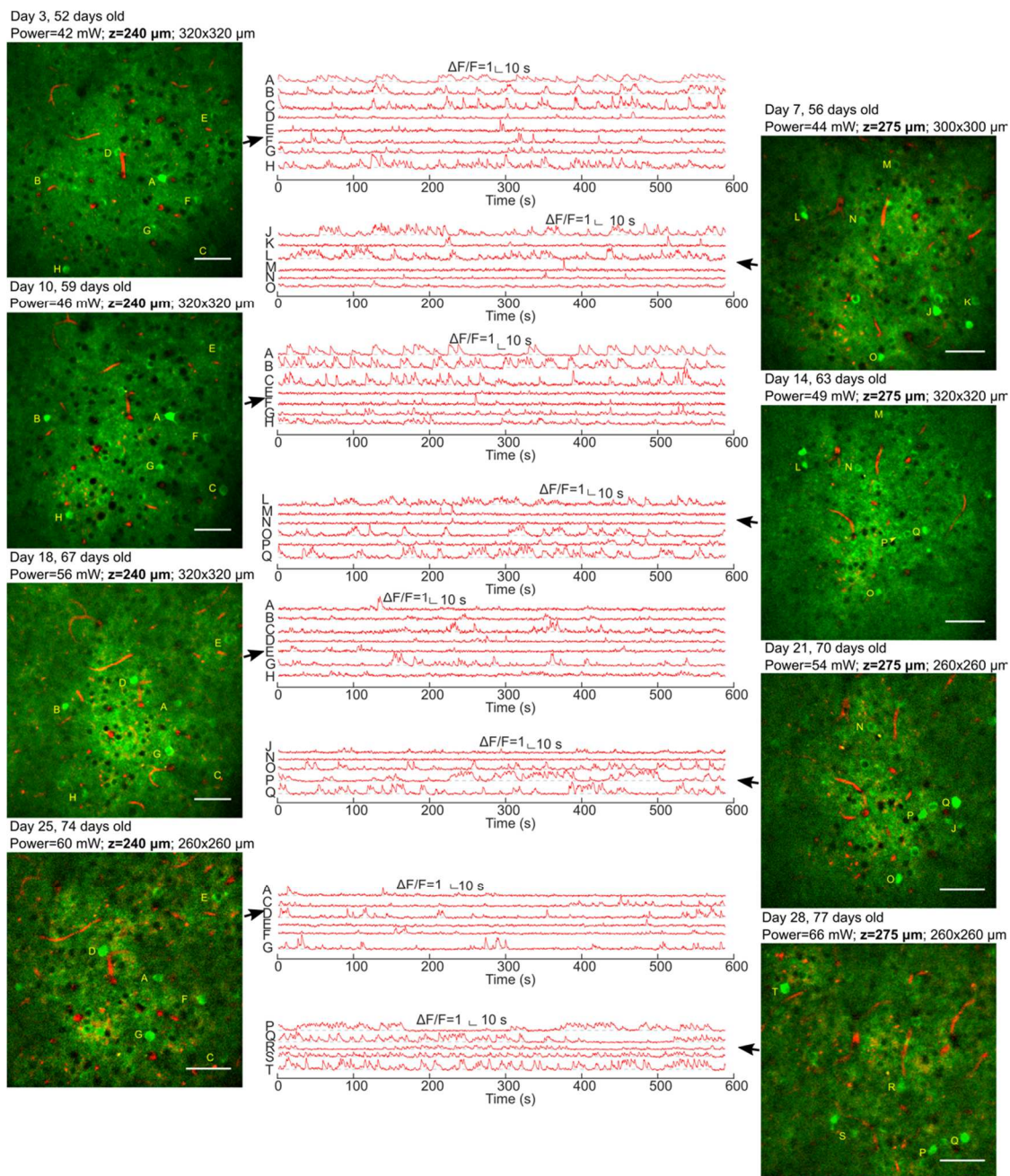


Figure 18 Longitudinal Through-skull Neuronal Activity Recording at the Same Locations in an Awake Animal over a Period of 4 Weeks

Spontaneous activity traces from cortical L2/3 neurons recorded in a GCaMP6s mouse under awake condition (*CamKII-tTA/tetO-GCaMP6s*,

female, 8-11 weeks old) over a period of 4 weeks after the skull preparation. The left panels show high resolution images of one recording site at 240  $\mu\text{m}$  cortical depth, and the right panels show another site at 275  $\mu\text{m}$  depth (the same site as in Figure 17f and g). Green: GCaMP6s fluorescence; red: THG; Scale bar, 50  $\mu\text{m}$ . THG visualizes the vasculature map, which was used to navigate to approximately the same location for recording. It is difficult to match the recording site exactly for each imaging session. Therefore, only a fraction of the neurons can be identified in multiple imaging sessions. These neurons are indexed alphabetically, and the same indices are used for all imaging sessions. The day since the skull preparation, the age of the mouse, the average power used for activity recording, the imaging depth, and the size of FOV are indicated at the top of each image. 8 recording sessions were performed at each site (4 at each site are shown). The middle panels show the activity traces of the indexed neurons, recorded at 8.49 Hz frame rate, and each was normalized to its baseline and low-pass filtered by a hamming window with 1.06 s time constant. The repetition rate for all imaging was 800 kHz. The thickness of the skull was about 120  $\mu\text{m}$ .

We performed longitudinal study and recorded from the same neurons on 8 different days over a period of 4 weeks after the initial skull preparation (Figure 18 and Figure 20a show longitudinal recordings from 3 sites at different depths). THG signal from the blood vessels was used to locate approximately the same imaging FOV for each recording session. Despite the long exposure time (cumulatively over 6 hours per recording site), no visible adverse effects had been observed on neuronal structure or activities, indicating the average power and the peak intensity were safe for imaging. We observed some degradation of skull transparency over time, as indicated by the power needed to image the same sites (e.g. 35-50% more power after 4 weeks, Figure

18). Nonetheless, successful recordings of neuronal activity were performed for all imaging sessions.

### 5.5 *The Limits of Three-photon Through-skull Calcium Imaging*

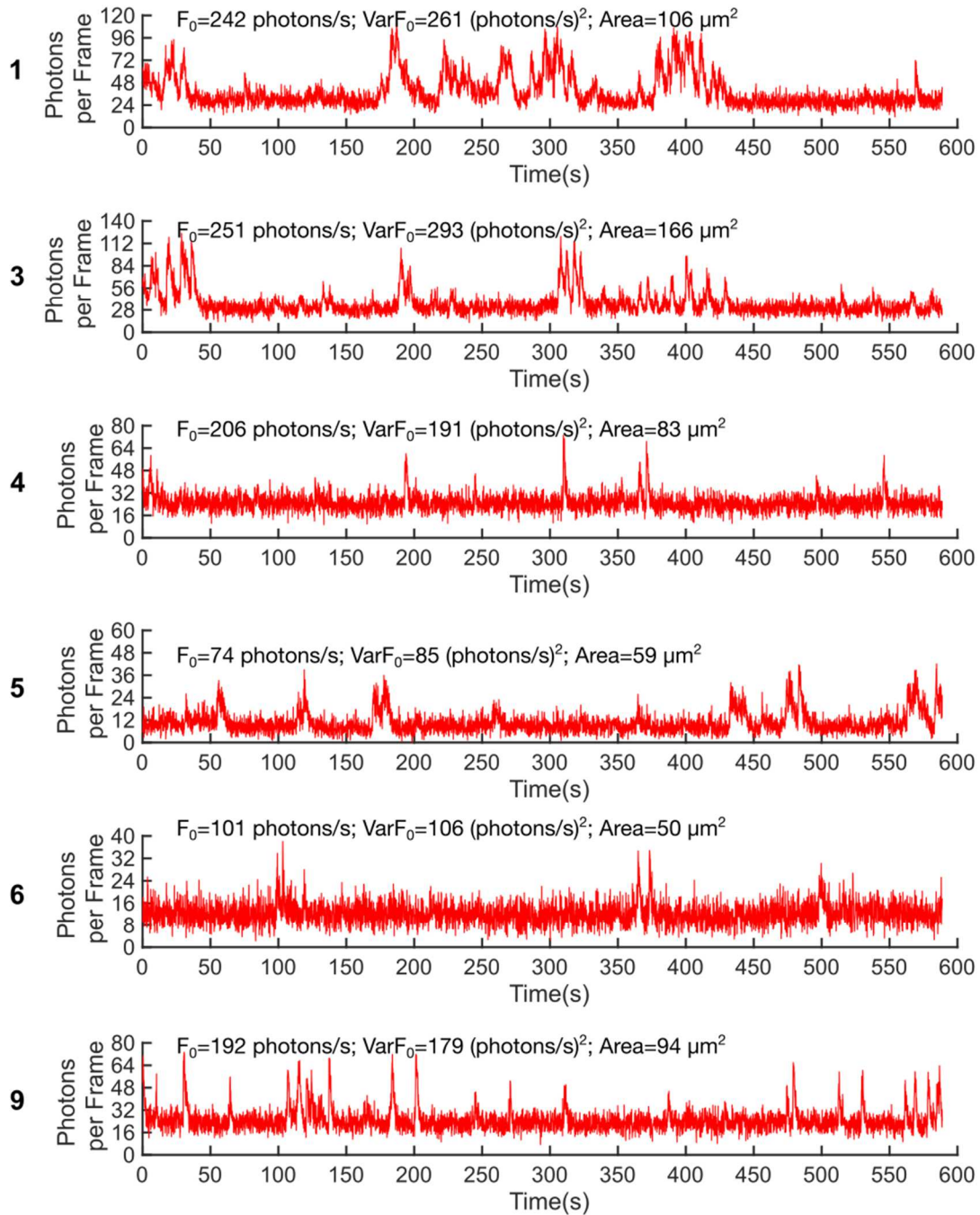


### Figure 19 Raw Data of Through-skull Neuronal Activity Traces

A subset of the activity traces in Figure 17g, representing neurons of different sizes, brightness, and activity patterns. The signal of each neuron (in photons/neuron/frame) was plotted against time. The data is recorded at 8.49 frames per second, without any temporal down-sampling or low-pass filtering. Fluorescence intensity was converted to photon counts per frame per neuron to confirm that the baseline fluctuations are mostly due to photon shot noise. The value of the measured mean ( $F_0$ ) and variance ( $\text{Var}F_0$ ) of the baseline fluorescence photon-count rate, and the areas of each neuron, are indicated above each trace. The index of each neuron is labeled to the left of each trace.

The absolute signal-to-noise ratio (SNR) of 3PM through-skull calcium imaging is comparable to typical 2PM calcium imaging through a cranial window, which can be ascertained by the raw photon counts (Figure 19). As discussed in Section 2.3, with shot-noise-limited optical detection and assuming that the sampling rate is sufficiently high relative to the response time of the indicator, a baseline signal strength  $F_0 \sim 100$  photons/neuron/s is required for GCaMP6s to yield  $\sim 93\%$  true detection and 7% false detection rate for an isolated single action potential.

As imaging depth increases, the  $\Delta F/F$  for through-skull 3PM appears to decrease due to increased background contribution (Figure 15d). To maintain the SNR and temporal resolution, the photon counts per neuron per second must be increased by either delivering additional power to the focus or reducing the repetition rate of the excitation (e.g., 400 kHz, Figure 20b and c), albeit at the expense of a reduced FOV or frame rate. The deepest activity imaging in this study was at 465  $\mu\text{m}$  below the

cortical surface (Figure 20).

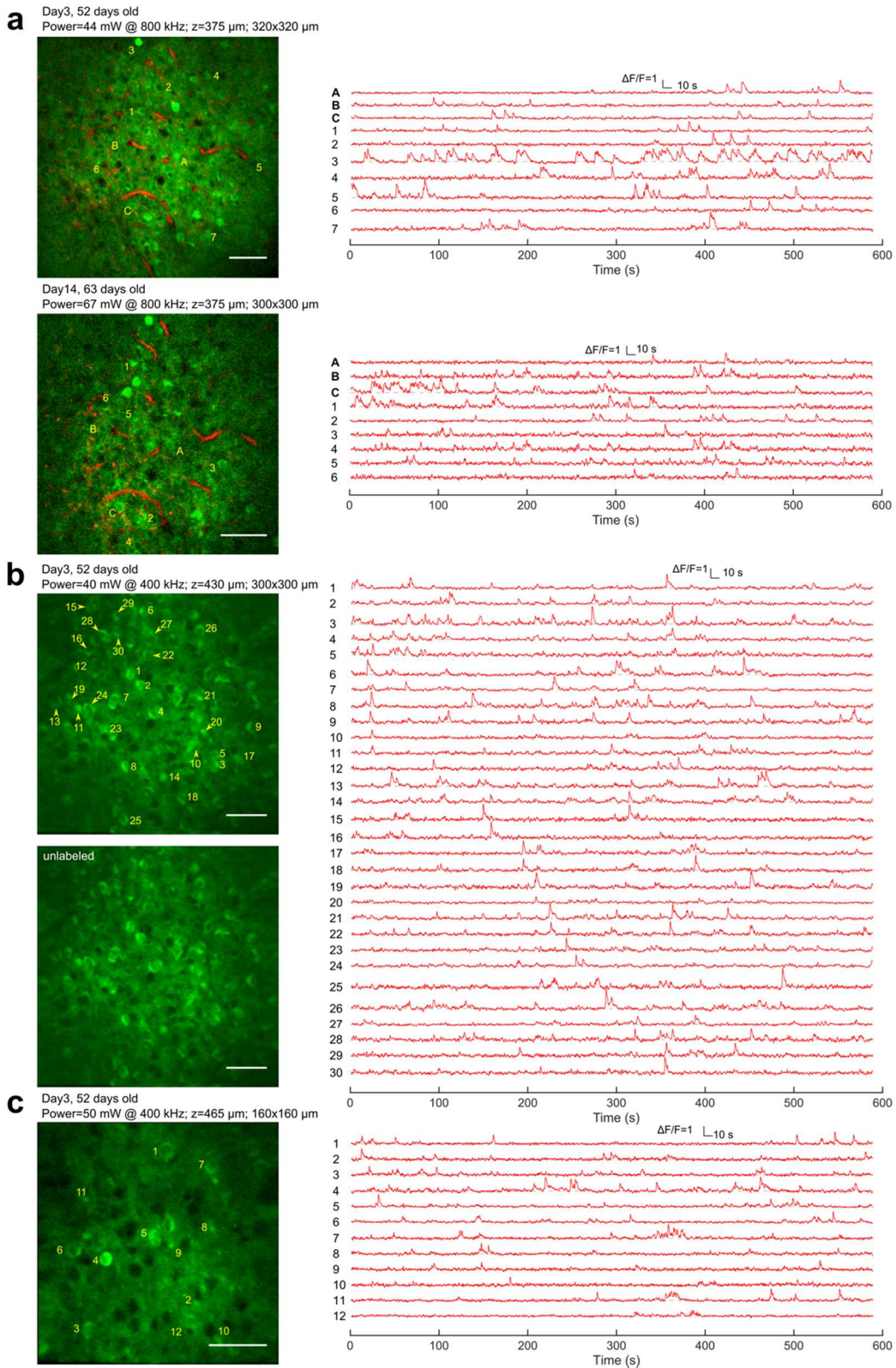


## Figure 20. Through-skull Neuronal Activity Recording in an Awake Animal in Deeper Cortex

Spontaneous activity traces from deeper cortical neurons recorded in a GCaMP6s mouse under awake condition (CamKII-tTA/tetO-GCaMP6s, female, 8-9 weeks old). Left panels show high resolution images of the recording site (green: GCaMP6s fluorescence; red: THG; Scale bar, 50  $\mu\text{m}$ ). The neurons are indexed for their corresponding time traces. The day since the skull preparation, the age of the mouse, the average power, the repetition rate, the imaging depth, and the size of FOV are indicated at the top of each image. The right panels show activity traces of the neurons, recorded at 8.49 Hz frame rate. The traces were normalized to their baselines and low-pass filtered by a hamming window with 1.06 s time constant. The thickness of the skull was about 120  $\mu\text{m}$ .

**a**, a recording site located at 375  $\mu\text{m}$  cortical depth observed in two imaging sessions 11 days apart. We leveraged the THG channel to visualize the vasculature map, which serves as the landmark for locating the same recording site. Due to small variations in each imaging session (e.g., mouse orientation, tilting, the finite focal depth, etc.), however, it is difficult to match the recording site exactly. Nonetheless, some neurons can be identified in both imaging sessions. These neurons are indexed alphabetically, and the same labels are used for both imaging sessions. Neurons only observed in one of the two imaging sessions are indexed numerically.

**b**, a recording site located at 430  $\mu\text{m}$  cortical depth. An additional image without any neuron indexing (unlabeled) is shown for better visualization of the image.

**c**, the deepest recording site of this study located at 465  $\mu\text{m}$  cortical depth.

The limits on FOV, temporal resolution, and imaging depth for activity recording are ultimately determined by the characteristics of the fluorescent probe, and the maximum allowable average power under the objective lens and peak power at the focus.

To estimate the safe range of average power, we performed immunostaining in the brains after imaging (Figure 21). The immunostaining results indicate that 60 mW average power under the objective lens at 400 kHz repetition rate did not cause measurable damage, while 120 mW at 400 kHz repetition rate caused activation of both heat shock protein 70/72 (HSP) and glial fibrillary acidic protein (GFAP). The former is upregulated by heat stress, and the latter signals astrocytic activation. The procedures followed ref. 41, with 30 minutes continuous exposure to laser scanning to ensure the temperature had reached steady state, and there was sufficient time for damage to take place. The animals were only perfused after 16 hours to allow enough time for immune response. These results are consistent with our longitudinal studies, where neurons remained viable after hours of exposure to as high as  $\sim 70$  mW under the objective lens at 800 kHz repetition rate. The thermal damage for through-skull imaging probably happens at a lower temperature than that for imaging through the cranial window where a significant portion of the skull is removed. Since the high thermal conduction through the cranial window plays a significant role in cooling the brain surface, and the maximum temperature rise occurred at hundreds of microns below the brain surface when imaging through the cranial window<sup>41</sup>.

Our immunostaining results (Figure 21) indicate that no measurable nonlinear tissue damage was detected with less than 10 nJ in the imaging plane. According to

the chronic imaging results (Figure 18), no neuronal damage was resulted from as high as 4 nJ pulse energy at the focus (imaging depths were between 240  $\mu\text{m}$  and 375  $\mu\text{m}$  with as high as 70 mW average power at 800 kHz repetition rate).

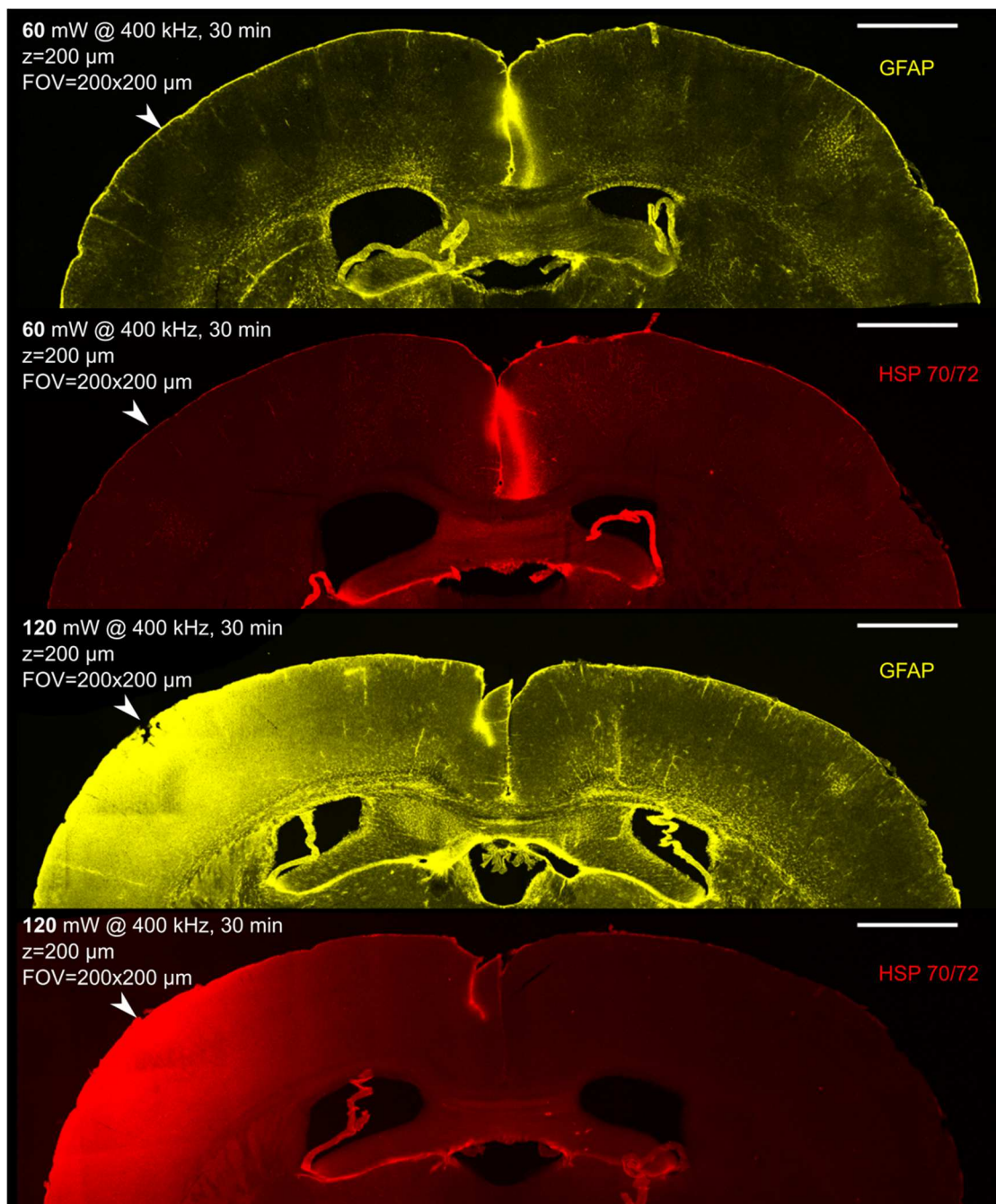


Figure 21. Immunolabeled Coronal Sections of Mouse Brains After Through-skull Imaging at 1320 nm.

The brain was imaged by 1320-nm 3PM operating at 400 kHz repetition rate. The imaging depth was about 200  $\mu\text{m}$  under the cortical surface, and the scanned area was 200x200  $\mu\text{m}$ , at the location of  $\sim$ 2.5 mm lateral and 1 mm caudal to the bregma point. The illumination continued for 30 minutes, and the brain was fixed after 16 hours. Scale bar, 1 mm.

Our results indicate that a 320  $\mu\text{m}$  x 320  $\mu\text{m}$  FOV in the cortical layer 2/3 is achievable for through-skull 3PM imaging of GCaMP6s without measurable tissue damage. To achieve larger imaging depth, the repetition rate or the FOV needs to be reduced to avoid thermal damage. While through-skull 3PM provides sufficient SNR for recording the activities with GCaMP6s in the shallow cortex, it requires much higher average and peak power than 2PM with cranial windows due to the combined effects of skull attenuation and the inefficient higher order nonlinear excitation. These power requirements ultimately limit the performance of through-skull 3PM. Therefore, 2PM imaging through cranial windows remains the preferred method if the experimental results are not expected to be affected by the craniotomy.

## **5.6 Conclusions**

We have demonstrated through-skull 3PM of mouse brain structure and function, with high spatial and temporal resolution, large FOV, and at significant depth. Furthermore, by comparing 2PM and 3PM at the same excitation wavelength, we show unequivocally that 3PE is necessary for imaging through the intact skull, regardless of the imaging depth and the labeling density. This work demonstrates the advantage of

higher order nonlinear excitation for imaging through a highly scattering layer, which is in addition to the previously reported advantage of 3PM in deep imaging of densely labeled samples. The demonstrated technique will open new opportunities for non-invasive studies of living biological systems.

## APPENDIX A

### MONTE CARLO SIMULATION FOR TISSUE TEMPERATURE RISE BY THREE-PHOTON MICROSCOPY

#### **Tissue Optical Heating Model: Overview**

The physical model of tissue heating is as follows: heat is generated by tissue absorption of excitation light, and removed by blood flow and more significantly by heat conduction through the cranial window. The cranial window has immense cooling effect by replacing the insulating tissue and bones with a highly conductive cover glass, especially with overlaying immersion water maintained at room temperature. In fact, the brain surface temperature can be as low as 32.4 °C without any radiative heating. At steady state under continuous laser scanning, tissue temperature increases with increased average laser power, until perturbation on neural behaviors happens when the maximum local temperature exceeds 38°C. For deep tissue imaging, especially beyond multiple mean free paths (MFPs), Monte Carlo simulation offers a simple and accurate way to calculate light intensity distribution, by taking account of photons experiencing zero, few, and multiple scattering events before absorbed. The spatial distribution of light absorption is then used as heat sources to calculate temperature distribution.

#### **Monte Carlo Simulation of Light Propagation and Validation of Tissue Optical Parameters**

Table 3. Optical Parameters of Grey Matter

Variable	Parameter	Wavelength	Value	Units
$\mu_a$	absorption coefficient	920	0.039	1/mm
		1320	0.11	1/mm
		1700	0.44	1/mm
$\mu_s$	scattering coefficient	920	6.7	1/mm
		1320	3.2	1/mm
		1700	2.1	1/mm
$g$	anisotropy coefficient	All	0.9	dimensionless
$n$	refractive index	All	1.36	dimensionless

Table 4. Derived Optical Parameters of Grey Matter

Parameter	Expression
reduced scattering coefficient	$\mu'_s = (1 - g)\mu_s$
light diffusion coefficient	$D = 1/3(\mu_a + \mu'_s)$
effective attenuation coefficient for diffusive light	$\mu_{\text{diff}} = \sqrt{3\mu_a(\mu_a + \mu'_s)}$
effective attenuation length for ballistic photons	$l_e = 1/(\mu_a + \mu_s)$

We used Monte Carlo simulation to calculate light propagation in the tissue, following the algorithm described by Stujenske *et al*<sup>62</sup>. Podgorski *et al*<sup>41</sup> adapted the algorithm for predicting tissue temperature change during multi-photon imaging, which agreed well with experimental measurements at the wavelengths of 800 nm, 920 nm, and 1064 nm. In order to simulate for 1320 nm and 1700 nm, we measured and estimated brain optical parameters at these wavelengths as follows: tissue absorption coefficients  $\mu_a$  are approximated with water absorption coefficients at 1320

nm and 1700 nm, since water dominates tissue absorption beyond 1000 nm, over other tissue composition or chromophores such as hemoglobin (Figure 1). Tissue scattering coefficients  $\mu_s$  were then calculated from our measured effective attenuation lengths according to  $l_e = 1/(\mu_a + \mu_s)$ , with  $l_e = 150 \mu\text{m}$  at 920nm,  $330 \mu\text{m}$  at 1320 nm and  $400 \mu\text{m}$  at 1700 nm. As a cross-validation, the calculated scattering coefficient at 1320 nm is close to that measured by Gebhart *et al* (i.e.  $3.0 \text{ mm}^{-1}$ )<sup>27</sup>. We assumed anisotropy factor  $g = 0.9$  and tissue refractive index  $n = 1.36$  for 920 nm, 1320 nm, and 1700 nm, since their variation in the wavelength range is small enough to have noticeable impact on simulation results. All the tissue optical parameters are summarized in Table 3 and Table 4.

For the Monte Carlo simulation, we under-filled the objective back aperture when randomly initializing photon distribution, according to relations:

$$\begin{aligned}
 w &= w_0 \sqrt{-1/2 \ln(X)} \\
 \theta &= \sin^{-1}(w/nf) \\
 r &= \tan(\theta) z
 \end{aligned}
 \tag{5}$$

Where  $X$  is a random variable drawn from a uniform distribution from 0 to 1,  $w_0$  is  $1/e^2$  beam radius of a Gaussian beam,  $w$  is the radial distance to objective optical axis of a randomly generated photon conforming the Gaussian beam profile mentioned above,  $f$  is the objective focal length,  $n$  is the refractive index of immersion water,  $z$  is the imaging depth in the sample. After the randomly generated photon is focused by the objective and reaches sample surface,  $(r, \theta)$  pair defines the radial coordinate of photon position and polar angle of momentum, both with respect to objective optical axis.  $\theta$  is calculated from  $w$  in the second equation according to the sine condition of

high NA objective. The objective (Olympus XLPLN25XWMP2, 25X) we used in this study has  $NA = 1.05$  and  $f = 7.2$  mm. The objective is under-filled with 70% of its back aperture matched to  $1/e^2$  beam diameter of a Gaussian beam (Section 2.1).

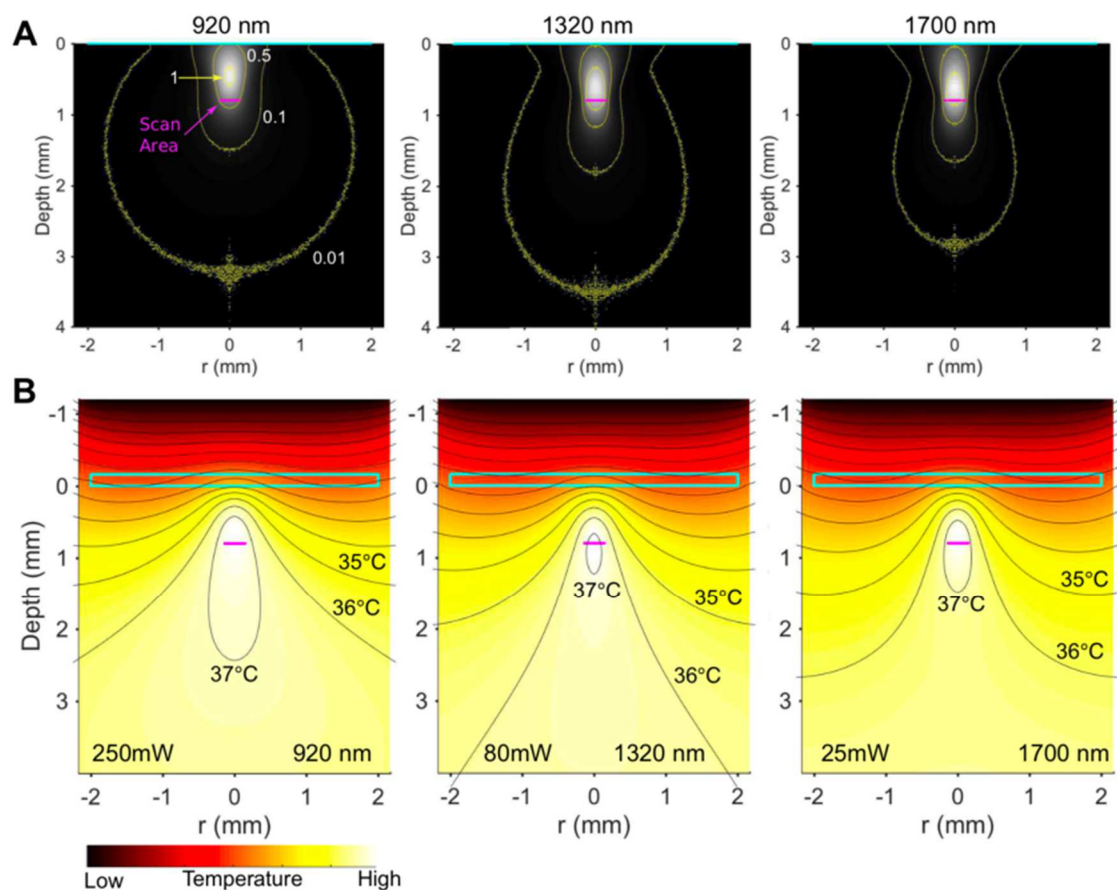


Figure 22. Monte Carlo Simulation Results of Light Intensity and Temperature Distribution in the Cortex

**a**, Light intensity maps with Iso-contour lines simulated for 920 nm, 1320 nm, and 1700 nm. Light is focused at 0.8 mm underneath the tissue surface with a 70% under-filled objective of 1.05 NA, and scanned telecentrically in a 0.3-mm diameter FOV. The light intensity maps are plotted in the vertical plane through the center of the scanned region, which is marked by horizontal pink lines. Four iso-contour lines are plotted in each intensity map, corresponding to absorption rates of  $P$ ,  $0.5P$ ,  $0.1P$  and  $0.01P$  per  $\text{mm}^3$

from inside to outside, where  $P$  is the total input power on sample surface. **b**, Temperature maps and isotherms calculated from their respective light intensity maps in (a) after 60 s of continuous scanning. Temperature is color-coded with heat colormap and plotted in the same plane as light intensity maps, with immersion water and cover glass added on the top (indicated by the cyan rectangles). The Isotherms are plotted with 1 °C increment with the highest 3 lines labeled with 37 °C, 36 °C, 35 °C. The average surface powers are denoted at the bottom-left of each plot, indicating approximately the highest allowable power to keep tissue temperature under 38 °C.

The calculated light intensity profile of 920nm, 1320nm, and 1700nm are shown in Figure 1a. The focal plane locates at 800  $\mu\text{m}$  below the brain surface, and the focus was scanned telecentrically in a FOV of 300  $\mu\text{m}$  diameter. The iso-contour lines depict the boundaries of equal intensity as well as light absorption rate  $\gamma$ , in the unit of  $\%/ \text{mm}^3$ , where % means the percentage of total input power on sample surface. For example, with total power  $P = 100 \text{ mW}$ , 0.01 or 1% in absorption rate translates to 1  $\text{mW}/\text{mm}^3$ . In Figure 22, four contour lines are plotted for each wavelength. The inner most contour line reflects absorption of mostly ballistic or snack-like photons, and among all wavelengths, 920 nm has the lowest absorption rate in the center of illuminated volume because of its small absorption coefficient. The most outside contour line reflects absorption of multiple-scattered photons, especially at large depth. Generally, a larger contour size indicates a lower absorption coefficient since the photons propagate far away before being absorbed. A more spherical contour indicates a higher ratio between scattering and absorption ( $\mu_s/\mu_a$ ), since photons are

sufficiently randomized in propagation direction before absorbed. The intensity profiles of 1320 nm and 1700 nm are similar, except that 1700 nm is more concentrated due to its higher absorption coefficient.

Table 5. Percentages of Excitation Photons for Different Destinations

	920 nm	1320 nm	1700 nm
Local tissue absorption	30	60	94
Back-scattered to window	25	9	3
Back-scattered to skull	20	9	1
Escaped*	35	22	2

\*Photons escape the simulation volume by traveling too far or too deep beyond 6 mm from the center of the cranial window or from the tissue surface.

One very important consequence of light scattering is that not all photons are absorbed within the illuminated volume and contribute to heating. According to the simulation results in Table 5, only 30% of photons cause local heating at 920 nm, while 25% are back-scattered to the cranial window, 20% to the skull, and 35% travel either too far or too deep. In comparison, as high as 94% of photons cause local heating at 1700-nm wavelength, due to a much lower scattering to absorption coefficient ratio. The photon destinations have very weak dependence on imaging depth, considering the fact that the angular components of the focused light are the same regardless of focal depth.

### **Heat Diffusion Model with Bio-heat Equation**

Using the light absorption rate as the heat source, the temperature distribution was then calculated by solving numerically bio-heat equation (6), identical to what previously used by Stujenske *et al*<sup>63</sup>:

$$\rho c \frac{\partial T(\vec{r}, t)}{\partial t} = k \nabla^2 T(\vec{r}, t) + \rho_b c_b w_b (T_A - T(\vec{r}, t)) + S_h(\vec{r}) + q_m \quad (6)$$

Where  $T(\vec{r}, t)$  is spatial-temporal temperature distribution,  $S_h(\vec{r})$  is radiative heat generation from Monte Carlo simulation, and the rest of parameters and their values are listed in Table 6, and are copied from ref. <sup>63</sup> for the ease of viewing. For example, Figure 22b shows the temperature distribution calculated from the light intensity distribution in Figure 22a of respective wavelength. According to the normal directions of isotherms, most heat dissipates through the cranial window instead of into the surrounding tissue. Consequently, the locations of the maximum temperature are generally below the point of the highest light intensity.

Table 6. Thermal and Mechanical Properties of Grey Matter<sup>62</sup>

Variable	Parameter	Value	Units
$\rho$	density	$1.04 \times 10^{-3}$	$\text{g/mm}^3$
$c$	Brain specific heat	$3.65 \times 10^3$	$\text{mJ/g}^\circ\text{C}$
$k$	Thermal conductivity	0.527	$\text{mW/mm } ^\circ\text{C}$
$\rho_b$	Blood density	$1.06 \times 10^{-3}$	$\text{g/mm}^3$
$c_b$	Blood specific heat	$3.6 \times 10^3$	$\text{mJ/g}^\circ\text{C}$
$w_b$	Blood perfusion rate	$8.5 \times 10^{-3}$	/s
$q$	Metabolic heat	$9.5 \times 10^{-3}$	$\text{mW/mm}^3$
$T_A$	Arterial temperature	36.7	$^\circ\text{C}$

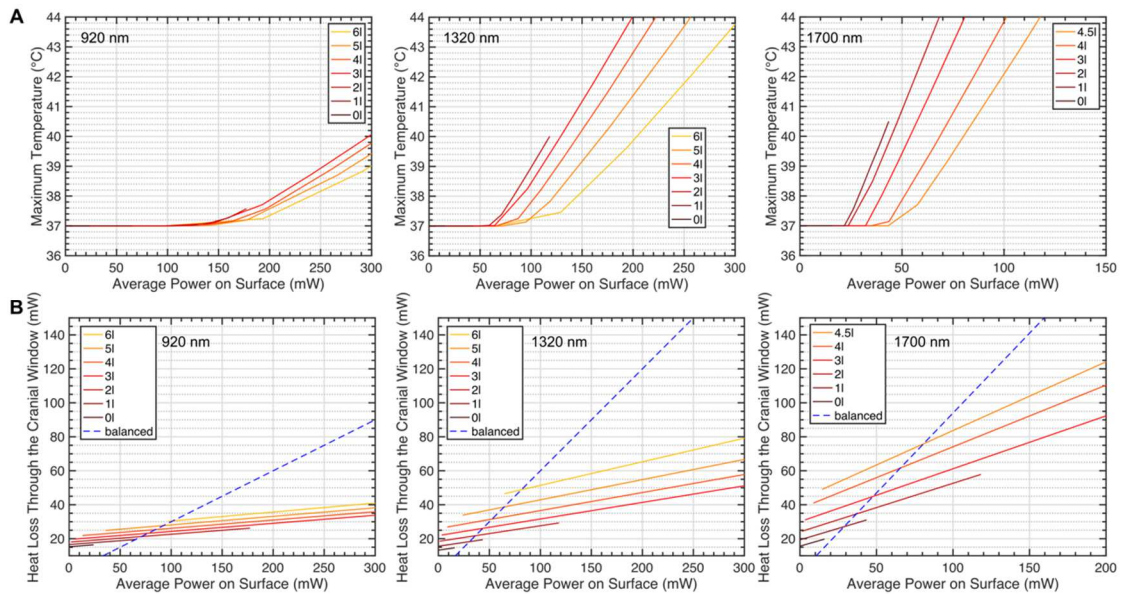


Figure 23. Prediction and Interpretation of the Critical Power for Tissue Temperature Rise

**a**, The maximum temperature versus the average surface power for different focal depths and wavelengths. The parameters of the Monte Carlo simulation are the same as in Figure 22. The focal depth is measured in the step of attenuation length, with  $l=150\ \mu\text{m}$  for 920 nm,  $300\ \mu\text{m}$  for 1320 nm, and  $400\ \mu\text{m}$  for 1700 nm.

**b**, The heat loss through the cranial window versus the surface power for different focal depths and wavelengths. The blue dashed lines (balanced) indicate the equilibrium between heat dissipation through the cranial window and absorbed locally by the tissue.

We calculated steady state temperature distribution at various focal depths (0-6 attenuation lengths until reaching the 2 mm objective work distance) and focal power (0.16- 16mW) for 920 nm, 1320 nm, and 1700 nm. Figure 23a shows the maximum

tissue temperature as the function of average input power on sample surface. The maximum temperature is evaluated as the average of the highest 0.1% temperature in the entire volume (a cylindrical volume of 6 mm radius and 6 mm height), and the surface power is defined as the excitation power incident on the tissue surface after the refraction through the cover glass. At each focal depth, the temperature only increases linearly with input power when it is greater than a critical value (We may define the critical power  $P_{38^{\circ}\text{C}}$  as the power it takes to exceed  $38^{\circ}\text{C}$ ).

The critical power can be understood by calculating the baseline heat dissipation through the cranial window: the fixed boundary temperature ( $25^{\circ}\text{C}$ ) at the objective front window establishes a temperature gradient across the cranial window and forces a constant heat loss. Estimated from the experimental measurements by Podgorski *et al*<sup>41</sup>, the temperature gradient can be as large as  $5^{\circ}\text{C}/\text{mm}$  close the brain surface in anesthetized mice with immersion water and the objective. Using the window clear diameter of 4 mm, and brain heat conductivity from Table 6, the cranial window causes about 33mW heat loss, which is about 5% of a mouse energy consumption (Ravussin). Given the conductive nature of the cortical tissue, its temperature will only increase when the input radiative power is greater than the constant heat loss. Figure 23b plots the calculated heat loss through a 4-mm diameter cranial window versus the surface power for some focal depths. The actual power absorbed locally by the tissue can be calculated by multiplying surface power with the local tissue absorption percentage in Table 5. The blue dashed lines in Figure 23b indicates the equilibrium between the power dissipated from the window and locally absorbed by the tissue. As more power deposited onto the sample surface, the whole

system eventually absorbs more power than the heat loss through the cranial window. As a result, the maximum temperature must rise to increase temperature gradient as well as heat dissipation. In Figure 23b, the crossovers between the equilibrium line and the heat dissipation curves give a good lower bound estimation for the critical power for 1320 nm and 1700 nm. The actual critical power is higher for 920-nm, since part of the heat is also dissipated radially without contributing to the local temperature rise, given the broad light intensity distribution determined by the high scatter absorption ratio ( $\mu_s/\mu_a$ ). As the focal depth increases, the critical power also increases, since the immersion water gets thinner and the heat dissipation through the cranial window increases. Incidentally, the maximum temperature rises more slowly with the surface power for larger focal depths, since there is more volume for heat dissipation along the radial direction. A larger cranial window also helps to reduce temperature rise by both facilitating heat dissipation and allowing more back-scattered photons to exit the window.

We can delineate the major optical damage mechanisms based the results in Figure 23. For 3PM imaging within 2 attenuation lengths with a typical laser repetition rate, the nonlinear damage almost always happens before thermal damage. For instance, 10 mW at the focus for 1320 nm will probably cause nonlinear damage with 10 nJ pulse energy assuming 1 MHz laser repetition rate, yet the temperature rise is negligible at within 2 attenuation lengths (Figure 23). For deep imaging beyond 2 attenuation lengths, thermal damage threshold can be the practical limit. For example, when imaging at 5 attenuation lengths with 1320-nm excitation wavelength, even 1 nJ at the focus leads to 150 mW average power on the surface, assuming 1 MHz

repetition rate, and the maximum temperature to exceed 39 °C.

## APPENDIX B

### MEASUREMENT OF OPTICAL POWER ABSORPTION BY IMMERSION WATER

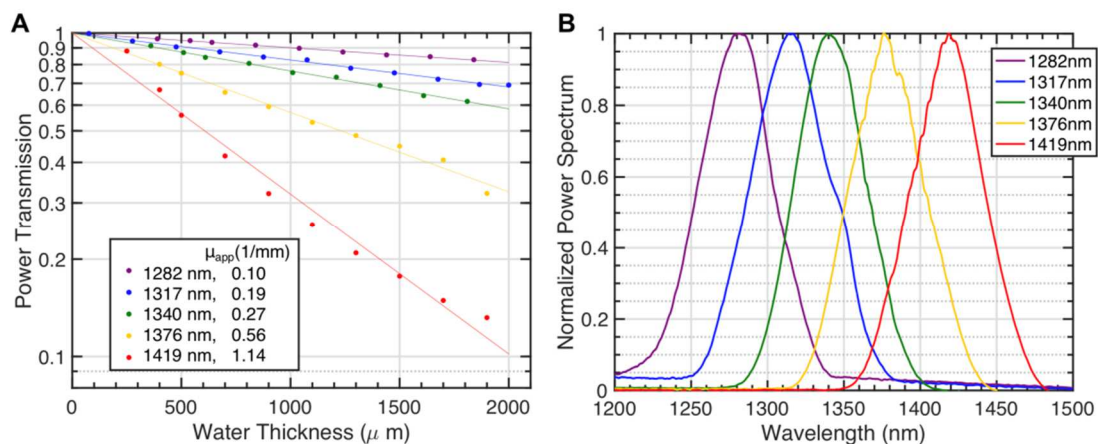


Figure 24. Light Attenuation with Immersion Water Thickness

**a**, Power transmission verses immersion water thickness under the objective (Olympus XLPLN25XWMP2, 25X, NA=1.05, 70% under-filled) for various idler spectra with central wavelengths from 1280 nm to 1420 nm. Each transmission curve is fitted with single exponential function for attenuation coefficient.

**b**, Light spectra of the transmission measurement in **(a)**.

The water absorption of optical power is much higher at longer wavelengths. For example, the absorption coefficient of the purified water at 1320 nm is about 10 times of that at 920 nm (0.11 verses 0.011 1/mm)<sup>25</sup>. In order to correctly calibrate the power at sample surface, we measured the light transmission through the objective immersion water by focusing light into an integration sphere, with its entrance pupil sealed by a cover slip (#1 thickness). By vertically translating the integration sphere,

we changed water thickness between the objective and the coverslip. We used the same objective as the rest of the paper, and the  $1/e^2$  beam size at the objective back aperture is about 11 mm. An integration sphere with a semi-conductor detector is necessary for its ability to measure low power of a couple mW and light at large angles. Figure 24a plots the power transmission as a function of immersion water thickness, for 5 spectra of different central wavelengths generated by the optical parametric amplifier, and each set of the data was fitted by an exponential function for the apparent attenuation coefficient ( $\mu_{app}$ ). As a reference, the water absorption coefficients at 1280, 1320, 1340, 1380, and 1420 nm are 0.10, 0.14, 0.18, 0.61, and 2.21 1/mm, respectively<sup>25</sup>. Different from the reference, we used much broader spectra (about 60-nm FWHM in Figure 24b), and a focusing geometry with large angle rays. Since the common way to measure the imaging power is by placing a power meter under an objective without immersion water, the measured apparent attenuation coefficients provide a way to calculate the actual power on the brain surface. For example, 100 mW at 1320 nm for 800  $\mu\text{m}$  focal depth translates to  $100\text{mW} \times \exp(-0.191/\text{mm} \times (2 - 0.8 - 0.16)\text{mm}) = 82\text{mW}$  on the brain surface, which is still a safe power to avoid thermal damage.

## APPENDIX C

### PROTOCOLS OF MOUSE BRAIN IMAGING THROUGH CRANIAL WINDOWS

#### ***Chronic Craniotomy***

For functional imaging in the mouse cortex, we imaged GCaMP6-labeled neurons in transgenic mice with high labeling density throughout the cortex (*CamKII-tTA/tetO-GCaMP6s*, 18–20 weeks). The mouse line was derived by crossing *B6;DBA-Tg(tetO-GCaMP6s)2Neil/J* and *B6;CBA-Tg(CamKII-tTA)1Mmay/J*.

Animals were anesthetized using isoflurane (3% in oxygen for induction and 1.5–2% for surgery to maintain a breathing frequency of 1 Hz). Body temperature was kept at 37.5 °C with a feedback-controlled blanket (Harvard Apparatus), and eye ointment was applied. Prior to surgery, glycopyrrolate (0.01 mg/kg body weight), dexamethasone (0.2 mg/kg body weight), and ketoprofen (5 mg/kg body weight) were injected intramuscularly. Dexamethasone and ketoprofen were also administered in two consecutive days following the surgery. We opened windows of 5 mm in diameter, centered at 2.5 mm lateral and 2 mm caudal from the bregma point over the somatosensory cortex. To reduce tissue growth under the window for chronic imaging, we used a coverslip assembly consisting of a donut-shaped coverslip (inner diameter 4.5 mm, outer diameter 5.5 mm, laser cut by Potomac Photonics) glued concentrically above a 5 mm diameter cover-slip (#1 thickness, Electron Microscopy Sciences; optical glue, Norland Optical Adhesive 68). The circular coverslip fit snugly into the open cranial window and was placed directly onto the intact dura. The donut coverslip on the top was glued to the skull (Krazy glue) to keep the inset window pressed

against the tissue, displacing as much room for potential tissue growth as possible. The window was further stabilized with dental cement covering the skull and the circular coverslip. In the case of a transgenic mouse, acute imaging happens immediately after the surgery, with the animal kept alive after imaging session. For all mice, chronic imaging happens after at least 5 d after the surgery after tissue inflammation disappears.

### ***Viral Transfection of Hippocampal Neurons***

For hippocampal imaging, we transfected neurons with AAV virus injection (synapsin promoter, AAV2/1 encapsulation,  $4.57 \times 10^8$  gene copies/mL; Penn Vector Core) in wild-type mice (N = 5, 8–10 weeks old, males, C57BL/6J, The Jackson Laboratories). The injection took place during the chronic cranial window implantation. The virus was diluted 1:4 in volume with saline and injected using a microinjector (M-10, Narishige) with tapered glass pipette (pipettes, 5-000-2010 Drummond; pipette puller, BV-10 Sutter Instruments) with inner diameter of  $\sim 20 \mu\text{m}$  at the tip. The pipette penetrated normal to the brain surface, and 64 nL virus solution was delivered for each depth at around 400  $\mu\text{m}$ ; 800  $\mu\text{m}$ ; 1,200  $\mu\text{m}$ ; and 1,600  $\mu\text{m}$ .

## APPENDIX D

### PROTOCOL FOR SKULL PREPARATION FOR CHRONIC IMAGING

1. Before the surgery, the animal is anesthetized with isoflurane (3% in oxygen for induction, and 1.5-2% during the surgery to maintain a breathing frequency around 1 Hz). The body temperature of the animal is kept at 37.5 °C with a feedback controlled blanket (Harvard Apparatus), and the eyes are covered with eye ointment.
2. Immediately after anesthesia, glycopyrrolate (0.01mg/kg body weight), dexamethasone (0.2mg/kg body weight), and ketoprofen (5mg/kg body weight) are administered intramuscularly. Glycopyrrolate and dexamethasone relieve respiratory distress and the buildup of mucus secretions in lungs during the surgical procedures when the animal is under anesthesia. Ketoprofen is an analgesic for pain reduction.
3. The anesthetized animal is fixed on a stereotaxic. Before any incision on the scalp, the hair must be cleanly removed with scissors and Nair™. The bald scalp is further cleaned and sterilized with alcohol wipes.
4. The scalp is cut open with surgical scissors and removed to expose both parietal plates as well as the bregma and lambda (Figure 25). Sterile saline is applied to the skull surface immediately after the exposure, and it is critical to keep the entire bone surface covered by saline to insulate it from air.
5. Fascia and connective tissue on the skull were gently removed with forceps and sterile wet cotton tips to avoid any internal bleeding inside the brain. The skull

should remain covered under sterile saline during the whole process. At this point, the whole skull should be quite transparent, with blood vessels underneath visible with sharp edges.

6. (Time-sensitive Step) Before applying any glue to the skull, the saline covering the skull is wiped dry with cotton tips. Before the bone turns opaque (usually happens within a couple seconds after exposing to the air), ultra-violet curable glue (Loctite 4305) is applied to the skull surface with a thin wooden tip. If the skull starts to turn opaque before applying the glue, recover it with saline to restore transparency, and then repeat this step. An example of opaque skull can be seen in Figure 1.
7. A sterile and dry round coverslip of 5-mm diameter (#1 thickness, Electron Microscopy Sciences) is placed on the skull, centered at 2.5 mm lateral, and 2 mm caudal from the bregma point. The coverslip is pressed closely against the skull surface by forceps to minimize the amount of glue between the coverslip and the skull. The glue is left to cure by itself for about 5 minutes without any ultra-violet light, during which time the skull transparency tends to increase visually. Afterwards, an ultra-violet light source (385-515 nm, Bluephase Style 20i, Ivoclar vivadent) is used to completely cure the glue, with roughly 1s on and 1s off for 3s. The coverslip is necessary to keep the glue layer as thin as possible (down to ~10  $\mu\text{m}$  at the thinnest part on the skull), and to form a flat interface to reduce aberration.
8. The exposed part of the skull surrounding the coverslip is further covered with dental cement. Figure 25 shows an example of successful preparation. For awake

imaging, a head-bar for head fixation during imaging is glued to the exposed parts of the skull surrounding the coverslip by metabond glue.

9. For chronic observation, dexamethasone and ketoprofen are also administered to the animal in two consecutive days following the surgery.

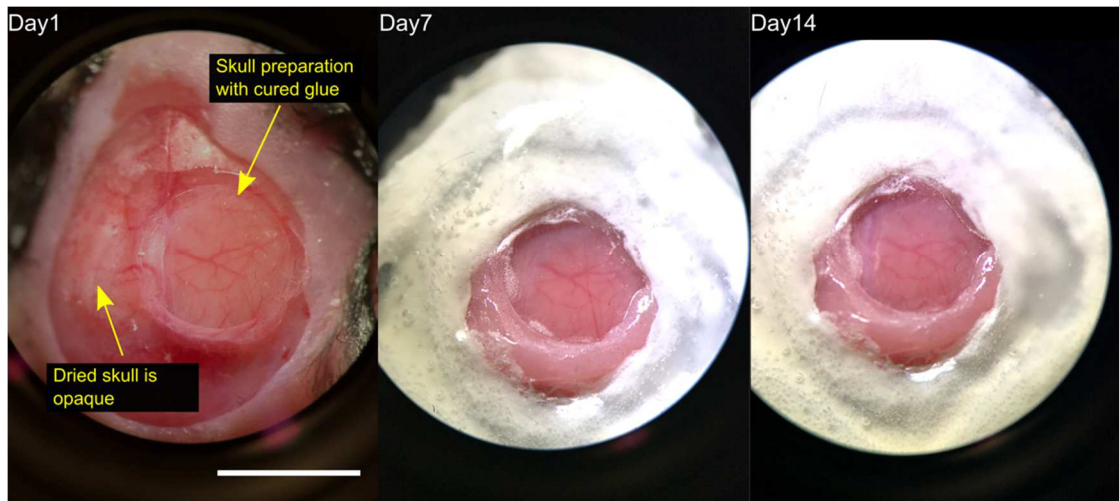


Figure 25. Visual Examination of the Skull Transparency after the Skull Preparation.

The bone surface was covered by Loctite 4305, and a #1 round coverslip (5 mm in diameter) was laid on top of it. The glue was cured by UV light. Day 1 was the day of the skull preparation. The images were taken under a stereoscope. Photos on day 7 and day 14 were taken after 2 and 3 recording sessions, respectively. Scale bar, 5 mm.

## REFERENCES

1. Denk, W., Strickler, J. H. & Webb, W. W. Two-photon laser scanning fluorescence microscopy. *Sci. p 34* **248**, 73–76 (1990).
2. Helmchen, F. & Denk, W. Deep tissue two-photon microscopy. *Nat. Methods* **2**, 932–940 (2005).
3. Wang, K. *et al.* Direct wavefront sensing for high-resolution in vivo imaging in scattering tissue. *Nat. Commun.* **6**, 1–6 (2015).
4. Katz, O., Small, E., Bromberg, Y. & Silberberg, Y. Focusing and Compression of Ultrashort Pulses through scattering media. **5**, 1–6 (2011).
5. Jang, M. *et al.* Relation between speckle decorrelation and optical phase conjugation (OPC)-based turbidity suppression through dynamic scattering media: a study on in vivo mouse skin. *Biomed. Opt. Express* **6**, 72 (2015).
6. Jacques, S. L. Optical Properties of Biological Tissues: A Review. *Phys. Med. Biol.* **58**, R37-61 (2013).
7. Kobat, D. *et al.* Deep tissue multiphoton microscopy using longer wavelength excitation. *Opt. Express* **17**, 13354–64 (2009).
8. Schuh, C. D. *et al.* Long wavelength multiphoton excitation is advantageous for intravital kidney imaging. *Kidney Int.* **89**, 712719 (2015).
9. Theer, P., Hasan, M. T. & Denk, W. Two-photon imaging to a depth of 1000 microm in living brains by use of a Ti:Al<sub>2</sub>O<sub>3</sub> regenerative amplifier. *Opt. Lett.* **28**, 1022–4 (2003).

10. Horton, N. G. *et al.* In vivo three-photon microscopy of subcortical structures within an intact mouse brain. *7*, 205–209 (2013).
11. Ouzounov, D. G. *et al.* In vivo three-photon imaging of activity of GCaMP6-labeled neurons deep in intact mouse brain. *Nat. Methods* **14**, 388–390 (2017).
12. Dombeck, D. A., Harvey, C. D., Tian, L., Looger, L. L. & Tank, D. W. Functional imaging of hippocampal place cells at cellular resolution during virtual navigation. *Nat. Neurosci.* **13**, 1433–1440 (2010).
13. Pilz, G.-A. *et al.* Functional Imaging of Dentate Granule Cells in the Adult Mouse Hippocampus. *J. Neurosci.* **36**, 7407–7414 (2016).
14. Hasegawa, A. & Tappert, F. Transmission of Stationary Nonlinear Optical Pulses in Dispersive Dielectric Fibers.1. Anomalous Dispersion. *Appl. Phys. Lett.* **23**, 142–144 (1973).
15. Gordon, J. P. Theory of the soliton self-frequency shift. *Opt. Lett.* **11**, 662–4 (1986).
16. Baker, P. F., Hodgkin, A. L. & Huxley, E. B. Depolarization and Calcium Entry in Squid Giant Axons. *J. Physiol.* 709–755 (1971).
17. Tank, D. W., Sugimori, M., Connor, J. A. & Llinás, R. R. Spatially resolved calcium dynamics of mammalian Purkinje cells in cerebellar slice. *Science (80-. )*. **242**, 773–777 (1988).
18. Grienberger, C. & Konnerth, A. Imaging Calcium in Neurons. *Neuron* **73**, 862–885 (2012).
19. Yang, W. & Yuste, R. In vivo imaging of neural activity. *Nat. Methods* **14**, 349–359 (2017).

20. Tischbirek, C., Birkner, A., Jia, H., Sakmann, B. & Konnerth, A. Deep two-photon brain imaging with a red-shifted fluorometric Ca<sup>2+</sup> indicator. *Proc. Natl. Acad. Sci.* **112**, 11377–11382 (2015).
21. Chen, T.-W. *et al.* Ultrasensitive fluorescent proteins for imaging neuronal activity. *Nature* **499**, 295–300 (2013).
22. Li, L. *et al.* Transgenic mice for intersectional targeting of neural sensors and effectors with high specificity and performance. *Neuron* **85**, 942–958 (2015).
23. Dana, H. *et al.* Sensitive red protein calcium indicators for imaging neural activity. *Elife* **5**, 1–24 (2016).
24. Welsh, A. J. & van Gemert, M. J. C. *Optical-Thermal Response of Laser Irradiated Tissue.* (2011).
25. Hale, G. M. & Querry, M. R. Optical Constants of Water in the 200-nm to 200- $\mu$ m Wavelength Region. *Appl. Opt.* **12**, 555 (1973).
26. Yaroslavsky, A. *et al.* Optical properties of selected native and coagulated human brain tissues in vitro in the visible and near infrared spectral range. *Phys. Med. Biol.* **47**, 2059–2073 (2002).
27. Gebhart, S. C., Lin, W. C. & Mahadevan-Jansen, A. In vitro determination of normal and neoplastic human brain tissue optical properties using inverse adding-doubling. *Phys. Med. Biol.* **51**, 2011–2027 (2006).
28. Bosschaart, N., Edelman, G. J., Aalders, M. C. G., Van Leeuwen, T. G. & Faber, D. J. A literature review and novel theoretical approach on the optical properties of whole blood. *Lasers Med. Sci.* **29**, 453–479 (2014).
29. Beaurepaire, E. & Mertz, J. Epifluorescence collection in two-photon

- microscopy. *Appl. Opt.* **41**, 5376–82 (2002).
30. Singh, A., McMullen, J. D., Doris, E. A. & Zipfel, W. R. Comparison of objective lenses for multiphoton microscopy in turbid samples. *Biomed. Opt. Express* **6**, 3113 (2015).
  31. Theer, P. & Denk, W. On the fundamental imaging-depth limit in two-photon microscopy. *J. Opt. Soc. Am. A* **23**, 3139–3149 (2006).
  32. Sinefeld, D., Paudel, H. P., Ouzounov, D. G., Bifano, T. G. & Xu, C. Adaptive optics in multiphoton microscopy: comparison of two, three and four photon fluorescence. *Opt. Express* **23**, 31472 (2015).
  33. Tuchin, V. V. Methods and algorithms for the measurements of optical parameters of tissues. *Tissue Opt. Light Scatt. Methods Instruments Med. Diagnosis* 143–256 (2000).
  34. Wilt, B. A., Fitzgerald, J. E. & Schnitzer, M. J. Photon shot noise limits on optical detection of neuronal spikes and estimation of spike timing. *Biophys. J.* **104**, 51–62 (2013).
  35. Macklin, John; Harris, T. Linear optical properties and two-photon action cross sections for GCaMP6f and RCaMP1he.
  36. Macklin, John; Harris, T. Three-photon action spectra of GCaMP6f, and the absorption coefficient of water.
  37. Cheng, L.-C., Horton, N. G., Wang, K., Chen, S.-J. & Xu, C. Measurements of multiphoton action cross sections for multiphoton microscopy. *Biomed. Opt. Express* **5**, 3427–33 (2014).
  38. Albota, M. A., Xu, C. & Webb, W. W. Two-photon fluorescence excitation

- cross sections of biomolecular probes from 690 to 960 nm. *Appl. Opt.* **37**, 7352 (1998).
39. Zinter, J. P. & Levene, M. J. Maximizing fluorescence collection efficiency in multiphoton microscopy. *Opt. Express* **19**, 15348 (2011).
  40. Tsai, P. S. *et al.* Plasma-mediated ablation: An optical tool for submicrometer surgery on neuronal and vascular systems. *Curr. Opin. Biotechnol.* **20**, 90–99 (2009).
  41. Podgorski, K. & Ranganathan, G. Brain heating induced by near infrared lasers during multi-photon microscopy. *bioRxiv* 057364 (2016). doi:10.1101/057364
  42. Wang, K., Liang, R. & Qiu, P. Fluorescence Signal Generation Optimization by Optimal Filling of the High Numerical Aperture Objective Lens for High-Order Deep-Tissue Multiphoton Fluorescence Microscopy. *IEEE Photonics J.* **7**, (2015).
  43. Yelin, D. & Silberberg, Y. Laser scanning third-harmonic-generation microscopy in biology. *Opt. Express* **5**, 169–75 (1999).
  44. McGonigle, P. Animal models of CNS disorders. *Biochem. Pharmacol.* **87**, 140–149 (2014).
  45. Holtmaat, A. *et al.* Long-term, high-resolution imaging in the mouse neocortex through a chronic cranial window. *Nat. Protoc.* **4**, 1128–1144 (2009).
  46. Yang, G., Pan, F., Parkhurst, C. N., Grutzendler, J. & Gan, W.-B. Thinned-skull cranial window technique for long-term imaging of the cortex in live mice. *Nat. Protoc.* **5**, 201–208 (2010).
  47. Drew, P. J. *et al.* Chronic optical access through a polished and reinforced

- thinned skull. *Nat. Methods* **7**, 981–984 (2010).
48. Dorand, R. D., Barkauskas, D. S., Evans, T. A., Petrosiute, A. & Huang, A. Y. Comparison of intravital thinned skull and cranial window approaches to study CNS immunobiology in the mouse cortex. *IntraVital* **3**, e29728 (2014).
  49. Thrane, V. R. *et al.* Paravascular microcirculation facilitates rapid lipid transport and astrocyte signaling in the brain. *Sci. Rep.* **3**, 2582 (2013).
  50. Jonckers, E., Shah, D., Hamaide, J., Verhoye, M. & Van der Linden, A. The power of using functional fMRI on small rodents to study brain pharmacology and disease. *Front. Pharmacol.* **6**, 1–19 (2015).
  51. Wang, X., Pang, Y., Ku, G., Stoica, G. & Wang, L. V. Three-dimensional laser-induced photoacoustic tomography of mouse brain with the skin and skull intact. *Opt. Lett.* **28**, 1739–1741 (2003).
  52. Wang, R. K. *et al.* Three dimensional optical angiography. *Opt. Express* **15**, 4083 (2007).
  53. Hong, G. *et al.* Through-skull fluorescence imaging of the brain in a new near-infrared window. *Nat. Photonics* **8**, 723–730 (2014).
  54. Silasi, G., Xiao, D., Vanni, M. P., Chen, A. C. N. & Murphy, T. H. Intact skull chronic windows for mesoscopic wide-field imaging in awake mice. *J. Neurosci. Methods* **267**, 141–149 (2016).
  55. Steinzeig, A., Molotkov, D. & Castrén, E. Chronic imaging through ‘transparent skull’ in mice. *PLoS One* **12**, e0181788 (2017).
  56. Park, J.-H., Sun, W. & Cui, M. High-resolution in vivo imaging of mouse brain through the intact skull. *Proc. Natl. Acad. Sci.* **112**, 9236–9241 (2015).

57. Zhao, Y.-J. *et al.* Skull optical clearing window for in vivo imaging of the mouse cortex at synaptic resolution. *Light Sci. Appl.* **7**, 17153 (2018).
58. Zhang, C. *et al.* A large , switchable optical clearing skull window for cerebrovascular imaging. *Theranostics* **8**, 2696–2708 (2018).
59. Wang, Y. *et al.* Aggregation-Induced Emission Luminogen with Deep-Red Emission for Through-Skull Three-Photon Fluorescence Imaging of Mouse. *ACS Nano* acsnano.7b05645 (2017). doi:10.1021/acsnano.7b05645
60. Ascenzi, A. & Fabry, C. Technique for Dissection and Measurement of Refractive Index of Osteones. *J Biophys Biochem Cytol.* **6**, 139–142 (1959).
61. Kobat, D., Horton, N. G. & Xu, C. In vivo two-photon microscopy to 1.6-mm depth in mouse cortex. *J. Biomed. Opt.* **16**, 106014 (2011).
62. Stujenske, J. M., Spellman, T. & Gordon, J. A. Modeling the Spatiotemporal Dynamics of Light and Heat Propagation for In Vivo Optogenetics. *Cell Rep.* **12**, 525–534 (2015).
63. Stujenske, J. M. *et al.* Modeling the Spatiotemporal Dynamics of Light and Heat Propagation for In Vivo Optogenetics Resource Modeling the Spatiotemporal Dynamics of Light and Heat Propagation for In Vivo Optogenetics. *Cell Rep.* **12**, 525–534 (2015).